Numerical Simulation and Modelling of the Dispersion in Tubing and Sample Loops Used in (Multidimensional) Liquid Chromatography

Jesús Ara Bernad

Master thesis submitted under the supervision of

Prof. Dr. Ir. Ken Broeckhoven

And the co-supervision of

Ir. Ali Moussa

Academic year

2020-2021

In order to be awarded the Master's Degree in

Chemical and Materials Engineering

Numerical Simulation and Modelling of the Dispersion in Tubing and Sample Loops Used in (Multidimensional) Liquid Chromatography

Jesús Ara Bernad

Master of Science in Chemical and Materials Engineering

Academic year: 2020-2021

Keywords: CFD, two-dimensional liquid chromatography, peak variance, modelling, sample loop.

Abstract

Over the last decade, two-dimensional liquid chromatography (2D-LC) has demonstrated great improvements in resolving power over conventional one-dimensional liquid chromatography (1D-LC), increasing the use of this technique in different fields, i.e., pharmaceutical analysis, environmental technology, or food industry. However, an impediment to the development of more methods is the lack of theoretical background.

In the present thesis, a mathematical model that predicts the dispersion (volumetric peak variance) experienced by a concentration step pulse along a sample loop was successfully built. The studied parameters were mainly the filling-elution flow rate ratio and the dimensionless elution time t^*_{elu}, which depends on the injection volume, geometry of the loop, diffusion coefficient of the species, and the elution flow rate. This mathematical model was based on breakthrough profiles obtained via computational fluid dynamics simulations in a wide range of conditions. The numerical results were compared with experimental data obtained from a collaborator (Prof. Stoll, Gustavus Adolphus College, Saint Peter, MN, USA)

Additionally, another mathematical model (from literature) was adapted to enable the prediction of the complete shape of the breakthrough profiles in the sample loop. The experimental elution peaks obtained from CFD simulations were fitted with this model, obtaining a list of parameters depending on the dimensionless elution time and the filling/elution flow rate ratio.

Finally, the effect of the hydrodynamic entry length was analyzed by performing some simulations with periodic boundary conditions and comparing it to a fixed mass inlet flow. Besides, the mass transfer entrance length was measured by changing the wall boundary condition from zero diffusive flux to a fixed mass fraction and analysing the concentration gradients along the radial direction.

Acknowledgments

I would like to express my sincere gratitude to prof. Ken Broeckhoven for his constant guidance and extensive explanations about the topic. I particularly appreciate the opportunity you gave to complete this thesis remotely in a difficult year for me. Also, Ali Moussa for introducing me in the CFD simulation field, providing me with all information and solutions I needed during these months. I would like to thank prof. Dwight Stoll, from Gustavus Adolphus College, for sharing his experimental results.

I am also grateful to my parents, for their encouragement and support all through my studies. Finally, I would like to mention my friend Pau Sintes for join me in this unforgettable adventure, and Lorenzo Toen for his invaluable assistance in Belgium.

Contents

List of Figures

List of Tables

List of Abbreviations

^{1}D	First-dimension column
1D-LC	One-dimensional liquid chromatography
^{2}D	Second-dimension column
2D-LC	Two-dimensional liquid chromatography
AC	Argentation chromatography
ASM	Active-solvent modulation
CFD	Computational fluid dynamics
FIFO	First-in-first-out
FILO	First-in-last-out
HILIC	Hydrophobic interaction liquid chromatography
HPLC	High-performance liquid chromatography
IEC	Ion exchange chromatography
IPA	Isopropanol
LCCC	Liquid chromatography under critical conditions
NP	Normal phase chromatography
RDS	Relative standard deviation
RP	Reversed phase chromatography
SEC	Size exclusion chromatography
SPAM	Stationary-phase-assisted modulation

List of Symbols

A	Height scaling factor	-
C_{center}	Axis concentration	kg/ m^3
C_i	Concentration	mol/m^3
C_{in}	Inlet concentration	kg/ m^3
C_{out}	Average outlet concentration	kg/ m^3
C_{wall}	Concentration at wall	kg/ m^3
d	Internal diameter	m

D_{mol}	Molecular diffusion coefficient	m^2/s
F_{elu}	Elution flow rate	m^3/s
F_{fill}	Filling flow rate	m^3/s
L_h	Hydrodynamic entry length	m
L_{inj}	Injection length	m
L_{loop}	Loop length	m
L_{MT}	Mass transfer entry length	m
MOM_i	i^{th} order moment of the elution profile	m^3
n_c	Peak capacity	-
p	Pressure	Pa
Re	Reynolds dimensionless number	-
R_{loop}	Loop radius	m
S	Surface	m^2
Sc	Schmidt dimensionless number	-
t	Time	s
t*	Dimensionless time	-
$\vec{v}$	Velocity vector	m/s
V	Volume	m^3
V’	Dimensionless volume	-
V_0	Position of the Gaussian peak	m^3
V_{fill}	Filling volume	m^3
V_{loop}	Loop volume	m^3
θ	Width of the square pulse	-
μ	Viscosity	kg/m/s
ρ	Density	kg/ m^3
σ	Standard deviation	m^3
σ_t^2	Time peak variance	s^2
σ_V^2	Volumetric peak variance	m^6
τ	Viscous shear stress	Pa
τ	Exponential decay time constant	m^3

1. Introduction

Over the last decade, two-dimensional liquid chromatography (2D-LC) has increasingly been used by a diverse group of users due to the need to separate samples of greater complexity, with better detection accuracy and in less time. This, supported by the limits associated with conventional one-dimensional liquid chromatography (1D-LC), is promoting the research and development in 2D-LC [1].

The pharmaceutical industry has been the principal user of 2D-LC, being helpful in pharmaceutical drug development stages for the separation of chiral molecules (which required a dedicated stationary phase) and biopharmaceutical separations (which contain a very high number of compounds). Nevertheless, 2D-LC is now more and more in use for analytical purposes in other fields like environmental technology, food analysis, and the chemical industry [2].

However, an impediment to the growth of this field is the lack of theoretical background, in order to know how various factors influence the separation and assisting in decision making during the development [3]. The use of simulation software for liquid chromatography can be useful in the optimization of the method variables, and therefore it can accelerate method development capabilities [4].

1.1 Two-dimensional liquid chromatography

2D-LC is a chromatographic technique where the injected sample is separated by passing through two different separation stages. A conventional separation takes place on the first-dimension (^{1}D) column, which can be isocratic or gradient elution. The effluent from the first system can optionally be analyzed in a detector and transferred to a sample loop which is located on an automatic switching valve. After the loop is filled, the valve changes its position, and the collected sample is injected onto the second-dimension (^{2}D) column with a different selectivity to improve the overall resolution. Finally, the sample passes through the second detector, and the 2D chromatogram is built. In Fig. 1 there is a schematic of the main components in a 2D-LC setup.

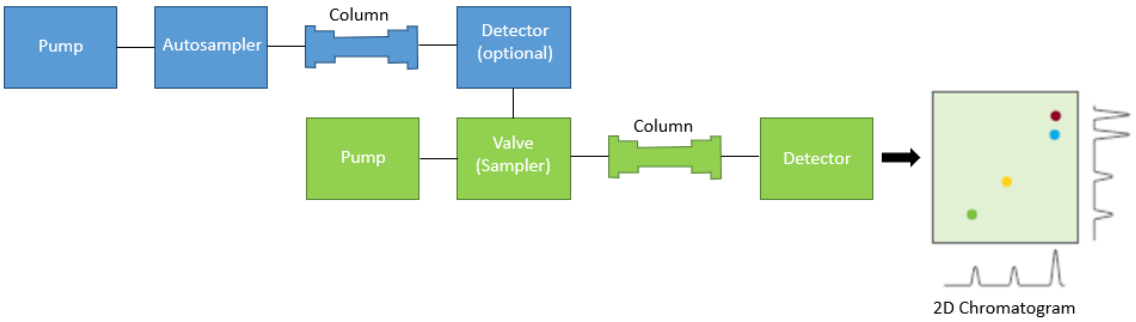

Figure 1. Schematic representation of a 2D-LC system with the first dimension in blue and the second dimension in green. Figure adapted from [1].

Typically, the ^{2}D column has a different separation mechanism, so the bands that are not clearly resolved in the ^{1}D column may be completely separated in the ^{2}D column if the ^{2}D separation mechanism is complementary. In general, one of the separation stages takes place in a reversed-phase column, whereas the other could be normal-phase, reversed-phase, HILIC, ion exchange, or size exclusion [1], although many other combinations are possible.

Two important parameters when designing a 2D separation are peak capacity and orthogonality. Peak capacity (n_c) is defined as the maximum number of peaks that can be separated over the separation window, and it can be estimated by dividing the gradient time by the average width of the peaks [5]. In multidimensional separations, the maximum peak capacity is given by the product rule:

$$n_c = n_{c,1} \cdot n_{c,2} \quad (1)$$

Where $n_{c,1}$ and $n_{c,2}$ are the ^{1}D and ^{2}D peak capacities. Thus, 2D-LC offers a higher separation power than in one dimension in orthogonal separations. A 2D-LC analysis is considered orthogonal if the separation mechanism is independent of each other and they provide complementary selectivities [6]. A great degree of orthogonality can be achieved by choosing the suitable mobile and stationary phases with respect to the physicochemical properties of the sample, including polarity, size, hydrophobicity, etc [7].

Besides the peak capacity and the orthogonality, the choice of the separation modes depends on the mobile phase since it must be compatible with both dimensions. In most pharmaceutic and biological applications, the most suitable combination is reversed-phase in both dimensions (RPxRP) [8]. This mode combination is not only the most versatile but also yields much higher peak capacities than others. In addition, the mobile

phase is fully miscible and has similar properties in both dimensions. The main drawback of the RPxRP method is the lack of enough orthogonal pairs of RP phases. These differences in column properties are summarized in Fig. 2.

Mode	IECxRP [45]	SECxRP [46]	NPxRP [47]	RPxRP [2]	HILICxRP [48]	HILICxHILIC [43]	ACxRP [49]	SECxNP [50]	SECxIEC [7]	LCCCxRP [51]
Orthogonality	++	++	++	+	+	-	++	+	+	++
Peak capacity	+	+	+	++	+	+	-	-	--	+
Peak capacity/ time	-	--	+	++	+	+	-	--	--	+
Solvent compatibility	+	+	--	++	+	++	+	+	+	-
Applicability	+	+	-	++	+	-	+	-	-	-
Score	4	3	1	9	5	2	2	-2	-3	2

Figure 2. Comparison of separation mode combinations for first and second dimensions in terms of orthogonality, peak capacity, solvent compatibility and applicability, from [1].

The increasing interest in 2D-LC is motivated by the impossibility to achieve the desired separation goals with 1D-LC, or only in an inefficient way. There are two main limits to 1D separations: very heterogeneous samples with thousands of compounds, and samples with chemically homogeneous groups of compounds that are difficult to resolve [9]. In this context, 2D-LC offers more potential resolving power and versatility, in a similar analysis time. However, this technique has some drawbacks: higher solvent consumption, more connections that imply an extra contribution to band broadening, data complexity, and higher sample dilution (low peak intensity) [10].

1.1.1 Implementations of 2D-LC

There are two different classes of ways in which 2D-LC technology can be implemented based on the number of peaks analyzed.

- Comprehensive 2D-LC: in comprehensive mode, everything that elutes from the ^{1}D is injected on the ^{2}D and analyzed by using very short gradients (see Fig. 3) [11]. This can be achieved by implementing two different loops in between the columns which work alternatively. The comprehensive setup offers additional

selectivity over the ^{1}D chromatogram, but the ^{2}D run time is limited to the sampling time, yielding a lower chromatographic resolution. Fast sampling times are requested to avoid loss of separation already obtained in the first column. In order to keep the sample volume injected into the second dimension and the valve switch time reasonable, the flow rate in the first dimension is often much smaller as in the second dimension, as well as the column diameter.

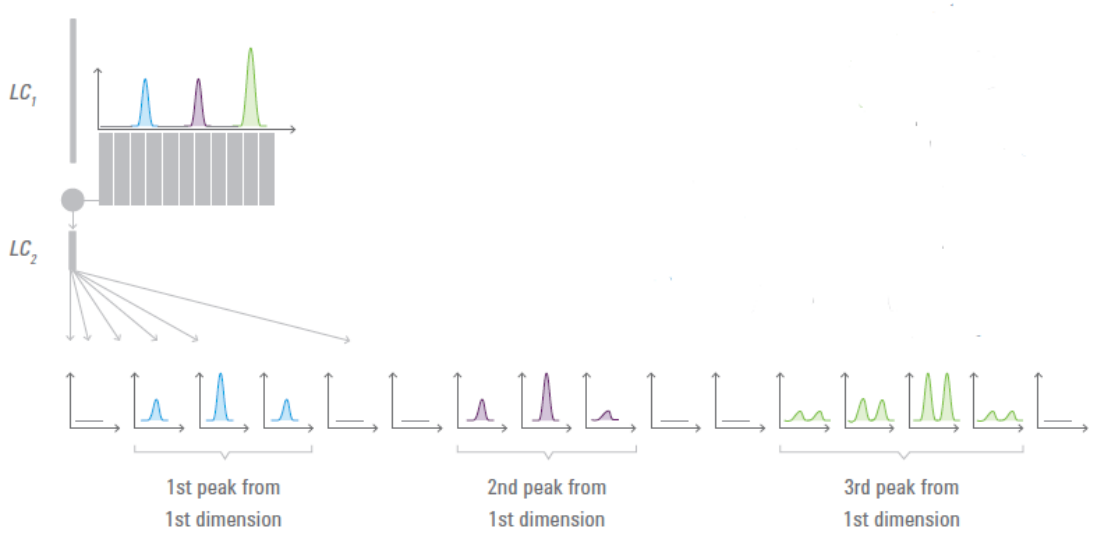

Figure 3. Comprehensive implementation of 2D-LC [1].

- Heart-cutting 2D-LC: in hearth-cutting chromatography, only a few parts of the ^{1}D column eluent are specifically collected in a sampling loop and transferred to the ^{2}D column, where another separation takes place (see Fig. 4) [1]. The main advantage of this technique is that the ^{1}D and ^{2}D run times are decoupled, so there are no time limitations on the second separation, allowing for a better optimization of the chromatographic resolution in the second column [12]. For this reason, it is a suitable method for not too complex samples, where the desired compounds have a similar retention behavior. However, only compounds that go to the ^{2}D column are analyzed and the information from the other cuts analyzed in the first column is lost.

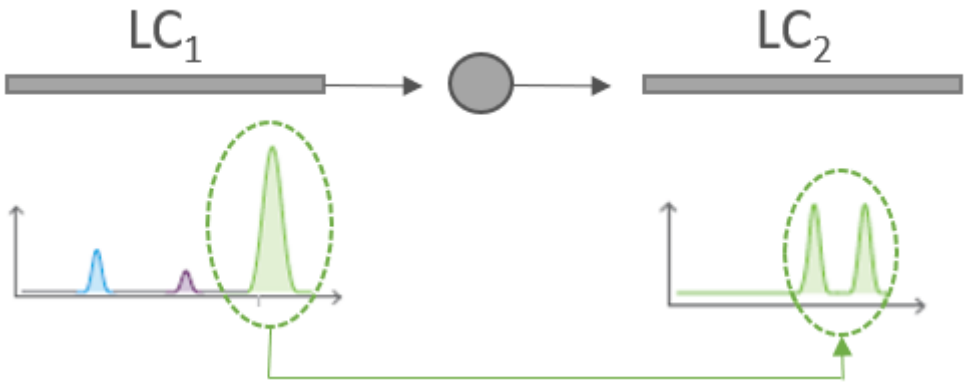

Figure 4. Heart-cutting implementation of 2D-LC. Only the green peak is collected in the loop and transferred to the second column. Figure adapted from [1].

Moreover, another classification can be established depending on the temporal implementation:

- Online 2D-LC: in this implementation, the elute from ^{1}D column is collected in a loop and directly injected into the ^{2}D column, while at the same time the ^{1}D column keeps working, meaning that the second separation is carried out in real-time. This system requires the ^{2}D separation to be completed during the time while the fraction is analyzed, collected, and restored the ^{1}D column to the initial conditions because the fraction is immediately transferred [13]. For this reason, the ^{2}D separation is time-constrained, resulting in limited resolving power. Nevertheless, this form of 2D-LC is the fastest and can be fully automated, without any operator intervention until all the data has been obtained. All in all, the total resolving power per unit run time is larger than offline or stop-and-go configuration.

- Offline 2D-LC: in offline 2D-LC, the fractions eluted from the ^{1}D column are stored indefinitely before the reinjection onto the ^{2}D column. In this system, there is no time limitation for either column and as a consequence, no high limit to the separation power. When larger peak capacities are needed, the offline method is suitable if very long analysis times are still acceptable [13]. Offline 2D-LC is frequently employed when the detector is a mass spectrometer.

- Stop-and-go 2D-LC: in stop-and-go implementation, the ^{1}D separation is run for a while, and when the effluent is collected, the ^{1}D is stopped and the fraction is analyzed in the ^{2}D. Afterward, the ^{1}D is resumed. This eliminates the time constraints of the ^{2}D but results in excessively long times and decreases the efficiency of the ^{1}D separation since the sample can diffuse along the axis of the column, even with the flow stopped [14]. In general, this method is the least used because of the overall analysis time.

1.1.2 Modulation valve

In a 2D-LC system, the two columns are connected by a modulation interface which ensures the collection of the ^{1}D effluent and allows the re-injection onto the secondary column. The most common tool in comprehensive LC is a 2-position/ 8- or 10-port high pressure switching valve equipped with two identical sampling loops that are alternately used [7]. As the ^{1}D effluent is sampled by one of the loops, the other one is being emptied onto the ^{2}D (see Figure 5: left). Once the valve switches, the contents of loop previously connected to the ^{1}D are injected to the ^{2}D, whereas the other loop is receiving effluent from the ^{1}D column (see Figure 5: right). This mode is known as passive modulation because the effluent is transferred unmodified. [2].

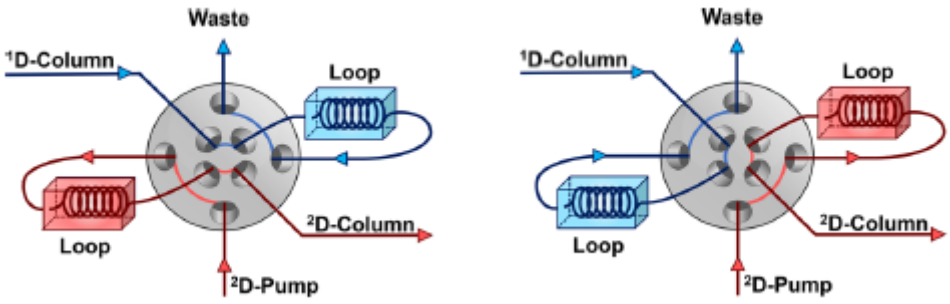

Figure 5. Scheme of an 8-port valve equipped with two loops, from [2]*.While the elute from the 1D column is being collected by one loop, the contents of the other loop are injected into the 2D column.*

Although the passive modulation strategy is simple and effective, there are certain limitations. Firstly, there may be compatibility issues between the two mobile phases, such as a significant different in solvent strength or viscosity, that result in peak deformation, or even peak splitting. Moreover, dilution factors are important

characteristics from the analyte detectability point of view. This dilution usually takes place at the injection of the ^{2}D column, being the main cause of loss in sensitivity and a decrease of the detection limits [2].

Over the last years, some modulation alternatives have been tested in order to overcome these issues. Active-Solvent Modulation (ASM) was developed to resolve solvent-compatibility problems. This interface split the flow from the ^{1}D in two portions, one is injected into the loop (as in passive modulation) and the other bypasses the loop directly to the ^{2}D column, acting as a diluent [15]. Another popular active modulation strategy is the Stationary-Phase-Assisted Modulation (SPAM), based on the use of low-volume trapping columns instead of storage loops. By this way, the analytes are retained in the stationary phase of the traps, whereas most of the solvent from the ^{1}D leaves the chromatographic system. Some advantages of SPAM are: improvement of sensitivity, no solvent incompatibility and reducing total analysis time. However, there is a significant risk of loss of analytes [2].

1.2 Computational fluid dynamics

Computational Fluid Dynamics (CFD) is a computer-based tool used to simulate systems that involve fluid flow, heat transfer, and other physical processes, i.e. chemical reactions. Nowadays, the role of CFD has become so important that it can be considered as the "third dimension" in fluid dynamics, in addition to pure experimental work and pure theory [16].

The CFD works by solving the equations of fluid flow over a designed geometry, with certain boundary conditions in that region. The physical aspects of any fluid flow are subjected to three fundamental principles: (1) mass conservations, (2) energy conservation, (3) Newton's second law [16]. CFD involves the application of these principles to a suitable model obtaining partial differential equations, which are replaced with discretized algebraic equations and are numerically solved at discrete points in time and/or space [17]. Among the different numerical methods used to discretize the partial differential equations, the most common are: the finite difference method, the finite element method (or finite volume), and the boundary element method.

There are some inherent drawbacks to the CFD calculations. They are only as valid as the mathematical model and boundary conditions are an accurate representation of the physical reality. In addition, the physical problem has to discretized in finite volumes rather than a continuum. The choice of a particular algorithm to obtain the solution can introduce truncation and round-off errors as well. But, all in all, CFD results are accurate for a very large number of applications as well as cost-effective [16].

In this thesis, the physical equations that describe the behavior of the mobile phase inside the sample loop are the continuity equation (Eq. (5)), the Navier-Stokes' equation (Eq. (7)), and the advection-diffusion equation applied to a species (Eq.(8)).

1.2.1 Fluid flow equations

To solve a fluid flow problem in the laminar regime, two equations have to be solved. Firstly, the mass conservation equation, also known as the continuity equation. This equation states that for a finite control volume fixed in space, the net mass flow out of the control volume V through a surface must be equal to the time rate of decrease of mass inside [16]. The mass flow across a fixed surface is:

$$\oiint \rho \, \vec{v} \cdot \vec{d}S \tag{2}$$

Where ρ is the density, $\vec{v}$ the velocity vector and S the surface. The time rate of decrease of mass inside V is then:

$$-\frac{\partial}{\partial t} \iiint \rho \, dV \tag{3}$$

Then, Eq. (2) must be equal to Eq. (3):

$$\oiint \rho \, \vec{v} \cdot \vec{d}S = -\frac{\partial}{\partial t} \iiint \rho \, dV \tag{4}$$

Applying the divergence theorem to the left hand of Eq. (4) and after some mathematical operations, it is obtained the continuity equation in conservation form [16]:

$$\frac{\partial \rho}{\partial t} + \vec{\nabla} \cdot (\rho \vec{v}) = 0 \tag{5}$$

When the flow can be considered incompressible, the density would be constant respect the time and position, leading to:

$$\vec{\nabla} \cdot \vec{v} = 0 \tag{6}$$

The second equation that must be solved is the momentum conservation equation known as the Navier-Stokes' equation, which is a set of equations that describes the motion of fluids. This equation is based on the application of Newton's 2nd law to the flow model. The general form of the equation an incompressible fluid is [17]:

$$\rho \frac{\partial \vec{v}}{\partial t} + \rho(\vec{\nabla} \cdot \vec{v})\vec{v} = -\vec{\nabla} p + \vec{\nabla} \cdot \tau + \rho \vec{f_b} \tag{7}$$

Where p is pressure, which is assumed isotropic, τ is the viscous shear stress tensor, $\vec{f_b}$ are the external forces per unit mass acting in proportion to a given control volume, i.e. the gravity.

1.2.2 Conservation of chemical species equations

In nature, the transport of species in fluids takes place through convection, which is the combination of advection and diffusion. Diffusion consists of the transport associated with random motions of the particles within the fluid, from regions of high concentration to low concentration, whereas advection is the movement of some material associated with the bulk flow under an external force [18].

Since the advection and diffusion are independent processes, it is possible to apply the conservation of mass to derive the advective-diffusion equation. This equation predicts the mass fraction of a chemical species at any position inside the studied domain. The general form of the advection-diffusion equation is [18]:

$$\frac{\partial C_i}{\partial t} + \vec{\nabla} \cdot (\vec{v} C_i) = \vec{\nabla} \cdot \left(D_i \vec{\nabla} C_i\right) + R_i \tag{8}$$

Where C_i is the species concentration, D_i the diffusion coefficient of the species, and R_i the sources or sinks of the concentration (chemical reaction). The first term $\frac{\partial C_i}{\partial t}$ is the accumulation contribution, the second term $\vec{\nabla} \cdot (\vec{v} C_i)$ describes the advection, whereas

the third term $\vec{\nabla} \cdot \left(D\vec{\nabla}C_i\right)$ corresponds to the diffusion mechanism, assuming laminar flow and no thermal diffusion inside the domain. The relative importance of the advection versus diffusion can be measured with the Peclet dimensionless number.

1.3 State-of-the-art

One of the weaknesses of 2D-LC is the precision of quantitation. Whereas in 1D-LC the relative standard deviations (%RDS) for replicate injections is less than 1%, in 2D-LC it can increase up to 10% [9]. This loss in precision is associated to the differences in the mobile phase compositions used in the two dimensions [19]. To optimize 2D-LC, a good knowledge of the shape of the actual plug being injected in the 2D column is required. Therefore, the process by which the effluent is transferred from the first separation stage to the second one by using a sample loop is particularly important.

In a theorical study, Moussa *et al*. [3] used CFD simulations to identify the factors that have a relevant influence on the analyte breakthrough from sampling loops. This showed that in the dimensionless volume ($V'=F_{fill} \cdot t/V_{fill}$) domain, the shape of breakthrough profiles only depends on a single dimensionless parameter:

$$t^* = \frac{V_{fill} \cdot D_{mol}}{F \cdot R_{loop}^2} \tag{9}$$

This dimensionless time represents the ratio of time needed to fill up or elute the sample to the characteristic time for radial diffusion. Moreover, it was reported that in most practical cases, loops are commonly filled up too much and thus they are losing a part of the sample collected from the ^{1}D due to the parabolic flow profile. Finally, they determined experimentally the effect of the coiling of the loop, since secondary flow effects are promoted under these conditions, resulting in a sharper breakthrough.

Deridder *et al.* [20] reported a CFD study of the band broadening that takes place in loop sample injectors and flow-through needles (which behave similar to small loops). The system worked according to the FILO principle (First In, Last Out), existing a holding time between the filling up and the elution step. It was shown that two different injection regimes exist: the convection regime (small t^*) and the diffusion regime (high t^*). In both

extremes of t^* the injection bands obtained are narrow, whereas in between the two regimes there is a peak in the volumetric variance of the injection bands, that is to say, broad bands. Very small t^*-values correspond to condition where the effects of the parabolic flow profile during filling can be compensated during elution because molecules do not have time to diffuse toward the wall before the flow is reversed to empty the needle, and therefore peak variance decreases. On the other hand, high t^*-values correspond to conditions where there is enough time for radial equilibration during filling and elution, and little molecules will trail behind by stay in the low velocity region near the wall, so peak variance decreases again. In addition, the hold time (time between sample uptake and injection) plays an important role in the variance of the peaks, and depends on the regime as well. However, in a loop working in online comprehensive 2D-LC, valve switching time is not relevant.

In another article, Wheatherbee *et al.* [4] modelled a set of experimental peaks that were fitted to a mathematical model (previously described by Forssén *et al.* [21]) to allow the prediction of the injection profile into the ^{2}D column, or in other words, the elution profile from the sample loop operating in FIFO mode. This mathematical model is the result of a convolution of a Gaussian peak with a square pulse with exponential decay (see Fig. 6):

$$h(V) = \frac{A}{2} \cdot [\mathrm{erf}\left(\frac{2V - 2V_0 + V_0\theta}{\sqrt{2}\sigma}\right) + \mathrm{erf}\left(\frac{2V_0 - 2V + V_0\theta}{\sqrt{2}\sigma}\right) + \exp\left(\frac{\sigma^2}{2\tau^2} + \frac{2V - 2V_0 + V_0\theta}{\sqrt{2}\sigma}\right) erfc(\frac{\sigma^2 - 2V\tau + 2V_0\tau + \theta V_0\tau}{\sqrt{2}\sigma\tau})] \quad (10)$$

Where A is the height scaling factor, V_0 the position of the Gaussian peak, $2\theta V_0$ the width of the square pulse, σ the standard deviation of the Gaussian peak, and τ the exponential decay time constant. The model showed a dependence of the injection profile on the flow rate and the loop size. The resulting injection profiles were used as input for ^{2}D separations, obtaining similar chromatograms as in the experiments.

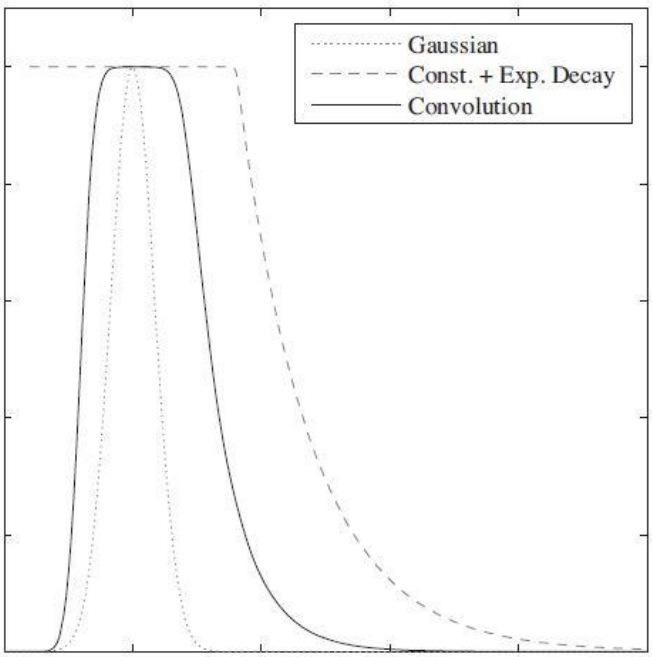

Figure 6. Convolution (solid line) of a Gaussian function (dotted line) and a square pulse with exponential decay (dashed line) [21].

1.4 Entrance region

When fluid low at a uniform velocity comes into contact with a solid surface, the fluid directly next to the wall will be stationary as a result of friction (no-slip condition) [22]. Due to the contact of this stagnant layer of liquid, the subsequent layers of liquid will also slow down in a gradually increasing thicker layer. This layer where the velocity increases slowly from zero at the wall to the uniform bulk velocity, in which the shearing viscous forces are significant, is called the boundary layer. In an open tube, the boundary layers gradually grow from the wall towards the centre. Outside of this layer is the irrotational (core) flow region, where the velocity profile remains constant in the radial direction and the viscous effects are negligible [22]. To keep the mass flow rate through the pipe constant, the velocity at the central axis of the pipe must increase, leading to a velocity gradient that develops along the pipe.

When fluid enters the pipe, the thickness of the boundary layer is zero, and as the fluid moves downstream, the thickness of the boundary layer increases resulting in significant velocity changes in the radial direction till the velocity becomes fully developed as the boundary layers overlap (the velocity profile becomes completely

parabolic). The region from the inlet to the point where the velocity profiles are fully developed is called the hydrodynamic entrance region, and the axial length is known as hydrodynamic entry length L_h. Beyond this length, the velocity profile remains constant and that region is the hydrodynamic fully developed region [23].

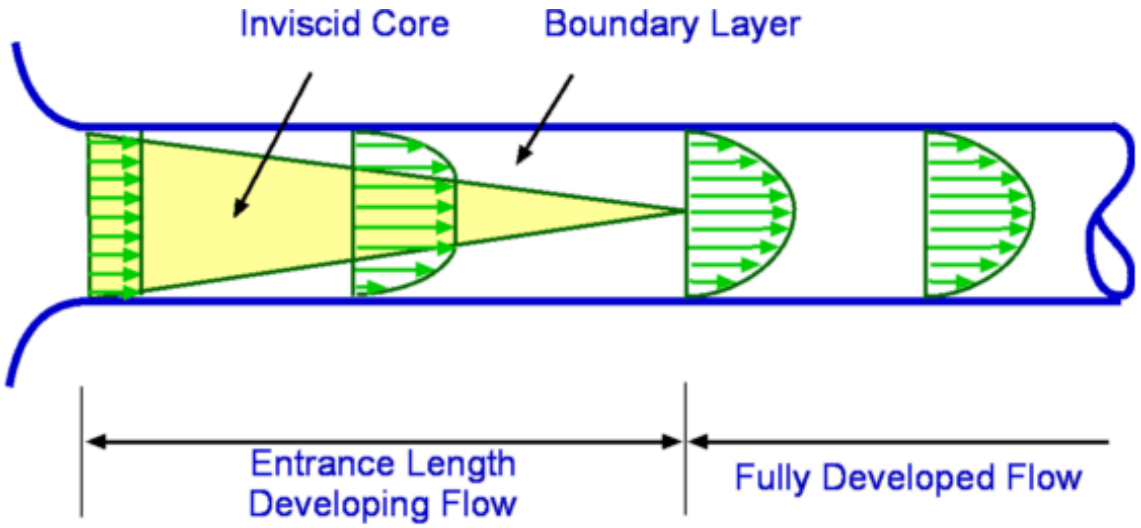

Figure 7. Different regions during the parabolic flow formation [23].

Understanding the entrance length is important for the design and analysis of flow systems. The entrance region presents a different velocity, temperature, or concentration profile than in the fully developed region [24]. In laminar flow, the hydrodynamic entry length, taken as the distance from the inlet to the 98% of the fully developed profile is given as [22]:

$$L_h = 0.05\, Re\, d \tag{21}$$

$$Re = \frac{u\, \rho\, d}{\mu} \tag{12}$$

Where d the pipe internal diameter and Re is the dimensionless Reynolds number that depends on the longitudinal velocity u, density ρ, internal diameter and viscosity μ. For small Re (~20), the hydrodynamic entry length is about the size of the diameter, but it depends linearly on the flow velocity.

In the same way as the velocity profile develops along the pipe, the concentration profile needs a certain length to become fully developed, which is called the mass transfer entry length L_{MT}. It is related to the hydrodynamic entry length and the Schmidt dimensionless number Sc:

$$L_{MT} = 0.05\, d\, Re\;\; Sc \tag{13}$$

$$Sc = \frac{\mu}{\rho\, D_{mol}} \tag{14}$$

Where D_{mol} is the diffusion coefficient Substituting Re and Sc by their definitions:

$$L_{MT} = 0.05\, d\, \left(\frac{\rho\, v\, d}{\mu}\right)\, \left(\frac{\mu}{\rho\, D_{mol}}\right) \tag{15}$$

Reordering the different parameters, Eq. (15) leads to:

$$L_{MT} = 0.05\, \frac{4}{\pi}\, \frac{F_{fill}}{D_{mol}} \tag{16}$$

With F_{fill} the filling flow rate. Introducing the dimensionless filling time t^*_{fill} (for the definition of t^*_{fill} see section 1.3) in Eq. (16), finally it is obtained:

$$L_{MT} = 0.05\, \frac{16}{\pi\, d^2}\, \frac{V_{fill}}{t^*_{fill}} \tag{17}$$

Where V_{fill} is the injection volume of the sample into the pipe. In the end, the mass transfer length will be inversely proportional to the dimensionless filling time t^*_{fill}, having important effects in the volumetric variance of experiments designed at low t^*_{fill} conditions.

2. Goals

The main goal of this project is to develop a universal mathematical model that predicts the dispersion experienced by a sample as it passes through a sampling loop between dimension columns in 2D-LC, operating in “First-In/First-Out” mode, for a wide range of experimental conditions (flow rates, diffusion coefficients of the species, injection volumes) and loop geometries, in absence of any other possible contribution to band broadening. These results are of high interest for the further development and optimization of two dimensional separations as these are the solute peaks that are injected in the second dimension. Due to the often occurring mismatch in solvent composition, these injected peaks are often diluted before injection in the second dimension, which of course further increases the injected volume which affects separation performance. Understanding the dispersion from the sampling loop alone, is therefore very useful for chromatographers to guide method development as it better allows to predict the injected peak width in the second dimension.

The model is built from results obtained via computational fluid dynamics simulations, and thereafter, verified with experimental data obtained from a collaborator (Prof. Stoll, Gustavus Adolphus College, Saint Peter, MN, USA). Moreover, some hypotheses are proposed and analysed to explain the mechanism behind band broadening under different regimes where convective or diffusive forces are dominant.

A secondary goal is to adapt a mathematical model found in literature, which allows the prediction of the complete shape of the breakthrough profile in the sample loop, validating its applicability under a wide range of experimental conditions.

3. Experimental procedure

3.1 Numerical simulations

3.1.1 Geometry

A straight sampling loop was modelled as a cylindrical tube with a radius (R_{Loop}) of 175 µm and a length (L_{loop}) of 374.1768 cm, resulting in a loop volume (V_{Loop}) of 360 µL. The breakthrough profiles were monitored at different V_{Loop} by placing monitor planes in the radial direction at distances corresponding to a volume of 10, 20, 30, 40, 60, 80, 100, 120, 160, 200, 240, 280 and 320 µL from the inlet. The geometry and boundary conditions are symmetric around the longitudinal axis, which allows simplifying the initial 3D geometry to a 2D rectangle with one axis of symmetry, an inlet, an outlet, and one wall, leading to a lower simulation time. Fig. 8 illustrates the simulation geometry (aspect-ratio scaled with 1/1000). The species distribution computed in the actual simulation geometry has been mirrored along the symmetry axis to view a full cross section of the sampling loop.

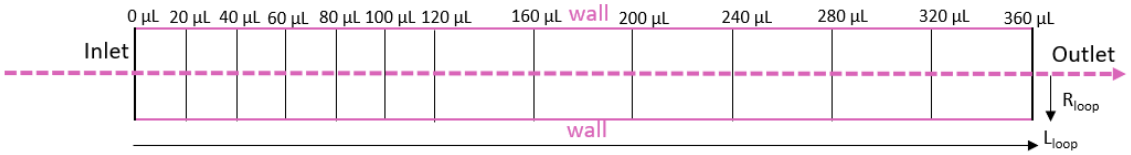

Figure 8. Sample loop geometry and the different monitor planes corresponding to the different loop volumes. Length scaled by a factor 1/1000.

3.1.2 Meshing

The geometry was meshed using a structured grid containing almost three million rectangular mesh cells. The total number of cell layers along the flow direction was 149670, whereas 20 cells were used along the radial direction. All cells had an axial length of 25 µm, while in the y-direction, the radial length varied between 1 µm near the wall and 30 µm near de symmetry axis, with a 1.195 height growth rate, to better capture the velocity and concentration gradients near the wall (see Fig. 9).

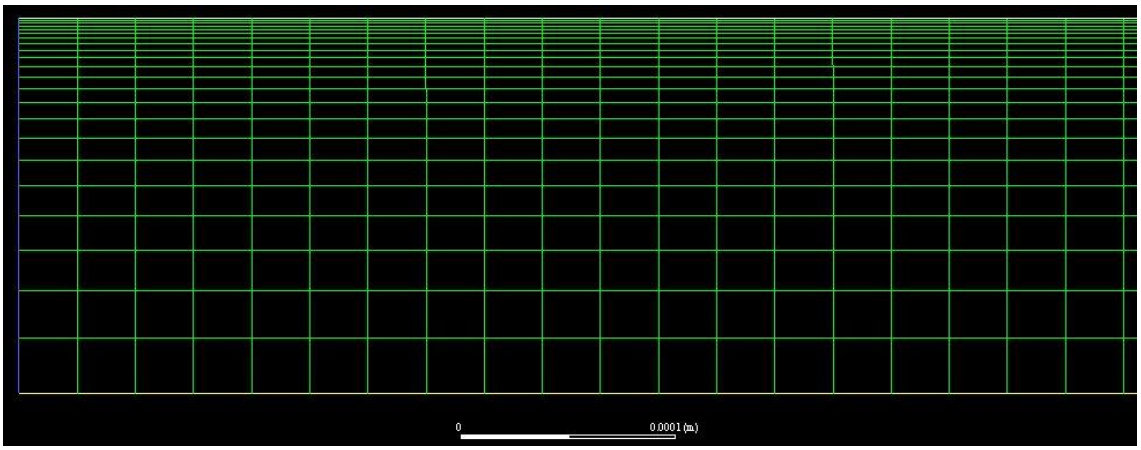

Figure 9. Plane view of the rectangular mesh model near the inlet, where the top side and bot side correspond to the wall and the symmetry axis respectively.

A grid check was performed by halving the width and height of all mesh cells, comparing the above mentioned grid size with one that used four times more cells. The difference in peak variance between both cases was 0.53% at t^*_{elu}=0.0002.

3.1.3 Simulation procedure

To simulate the filling and eluting step, a simulation procedure was used that consisted of 4 separate steps. Firstly, the steady-state velocity profile of the mobile phase in the sample loop was solved. Afterward, the transient concentration field was calculated in combination with the previous velocity field, resulting in a step change in concentration (C_{in}=0.01) at the inlet x=0-plane (=filling step). In the third step, the mass flow velocity is changed according to the F_{elu}/F_{fill} ratio, and the steady-state velocity profile is solved again with the elution conditions. Finally, starting from the concentration field obtained at the end of step 2, the concentration field was again calculated, but with zero inlet concentration and the new velocity field (=eluting step). An example of the concentration profiles during steps 2 and 4 can be seen in Fig. 10.

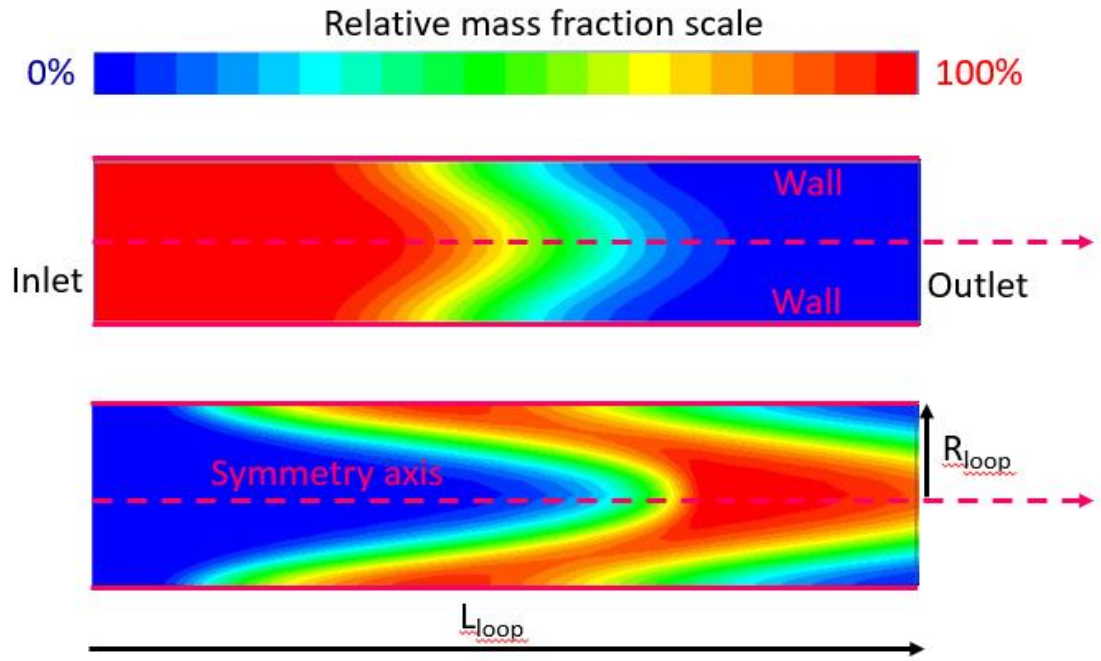

Figure 10. Simulated species profiles, F_{fill}=0.25 ml/min, F_{elu}=2 ml/min, D_{mol}=1x10^{-9} m^2/s, V_{loop}=160 µL, R_{loop}=175 µm, the length has been adjusted by a scaling factor of 1/1000. The top profile corresponds to the filling step (V_{fill}=80 µL, 19.2s) and the lower profile corresponds to the eluting step (V_{elu}=80 µL, 3s).

In the case of a different simulation where the geometry and flow rate are kept constant, the steady-state velocity profiles could be reused, even with different molecular diffusion coefficients or injection volumes.

3.1.4 Boundary conditions

The top side wall was assigned a no-slip boundary condition and a zero normal concentration gradient boundary condition. At the symmetry axis, a zero normal gradient was applied for both the concentration and the velocity field.

During the filling step, the left side of the capillary was treated as a mass flow inlet with a step function in mass fraction C_{in}=0.01, while on the right side a pressure outlet with a zero-gauge pressure and zero species mass fraction was applied. The F_{Fill} used was between 0.06 ml/min and 2.40 ml/min. The filling time was always chosen ensuring a maximum filling fraction of 0.5, since the loop can only receive an analyte volume equivalent to half of the V_{loop} before the molecules moving through the central streamline elute at the sample loop outlet [3]. To simulate the elution step, the inlet

concentration was changed to 0 and the F_{Fill} was replaced by F_{elu} (depending on the ratio F_{elu}/F_{fill}), keeping every other parameter as before. Moreover, some simulations were performed with a periodic boundary condition between the inlet and outlet, resulting in a fully-developed flow along the entire loop.

The different t^*-values and F_{elu}/F_{fill}-values considered in this thesis were the results of different combinations of inlet and outlet flow rates, diffusion coefficients, and loop volumes. The properties of the mobile phase are summarized in Table 1. The mobile phase is always assumed to be the same during filling and elution step.

Table 1. Physicochemical properties of the mobile phase used in the simulations.

Property	Liquid-water	Specie
Density	998.2 kg/m^3	998.2 kg/m^3
Viscosity	1.003x10^{-3} kg/(m·s)	1.003x10^{-3} kg/(m·s)
Molecular weight	18.0152 kg/kmol	18.0152 kg/kmol
Diffusion coefficient		[10^{-9} – 10^{-11}] m^2/s

3.1.5 Post-processing

Breakthrough concentration profiles were obtained at the outlet during the elution step by recording at each time step the flow rate average concentrations $C_{out}(t)$, defined as:

$$C_{out}(t) = \frac{\oiint u_s c_s dS}{\oiint u_s dS} \tag{18}$$

With u_s the local axial velocity across the monitor plane, c_s the local analyte concentration, and S the surface area of the monitor plane. The breakthrough profile was created by plotting $C_{out}(t)/C_{in}$ as a function of the time t or the normalized volumetric equivalent of the time V', defined as:

$$V' = \frac{F_{fill} \cdot t}{V_{loop}} = \frac{V_{fill}}{V_{loop}} \tag{19}$$

From the elution profile through a determined monitor plane, the volumetric peak variance σ_v^2 was calculated via the method of moments as it follows:

$$MOM_i = \int_0^{t_f} C_{out}(t) \cdot t^i \cdot dt \tag{20}$$

$$\sigma_t^2 = \frac{MOM_2}{MOM_1} - \left(\frac{MOM_1}{MOM_0}\right)^2 \tag{21}$$

$$\sigma_V^2 = \sigma_t^2 \cdot F_{elu}^2 \tag{22}$$

Where MOM_i is the i^{th} order moment of the elution profile, σ_t^2 the time peak variance, and t_f the at which $C_{out}(t)/C_{in}$ drops to 0.001, which is also a cut-off feasible to integrate the experimental elution profiles due to noise present on the baseline.

3.1.6 Solver settings

To determine the velocity and concentration fields, the conservation equations for mass and momentum and the convection-diffusion equation were solved by using the finite volumes solvers of Ansys Fluent with double precision. In order to solve the steady-state velocity fields, the pressure-based coupled solver with second order upwind spatial momentum discretization and second order spatial pressure discretization was used. When solving the transient concentration fields, first order upwind spatial discretization and second order implicit temporal discretization were used. The Least Squares Cell Based method was used to evaluate the gradients.

3.1.7 Software and hardware

All simulations were performed with Ansys Fluent 19.0 or 18.2 software on Dell Power Edge R210 Rack Servers, with an Intel Xeon x3460 processor (clock speed 2.8 GHz, 4 CPUs) and 16 Gb, 1333 MHz RAM running Windows server edition 2008 R2 (64-bit) as an operating system. Simulation time to calculate the flow was a maximum of 2 hours and the elution step took from some hours in F_{elu}/F_{fill}=80 to one week in F_{elu}/F_{fill}=1.

3.2 Experimental elution profiles

The experimental part was carried out by Prof. Dwight Stoll's group at Gustavus Adolphus College (Minnesota, USA). A schematic of the instrument setup used to obtain the breakthrough profiles is shown in Figure 11. All instrument modules were from Agilent Technologies (Waldbronn, Germany): an 8-port/2-position switching valve (p/n: 5067-4214), two 1290 High Speed Pumps (G7120A), a diode-array UV absorbance detector (G7117A). The valve was used in "First-In/First-Out" (FIFO) mode.

Uracil and isopropanol (IPA, HPLC Grade ≥ 99.9%) was purchased from Sigma-Aldrich (St. Louis, MO). Water was purified using a Milli-Q water purification system (Billerica, MA).

Elution profiles were measured using a 84.1+/- 0.7 µL test capillary. For each flow rate studied, experiments were performed twice: once with the capillary coiled and once with the capillary straight. The procedure is as follows: while the Pump 1 was connected to the test capillary, a 10 µg/mL pulse of uracil in 50/50 IPA/water (v/v) was directly injected into the 8-port switching valve and filled with a desired volume (around 40 µL). Afterwards, the valve was switched so that the Pump 2 was connected to the loop capillary and data were collected, whereas the loop was flushed. This process was repeated 6 times.

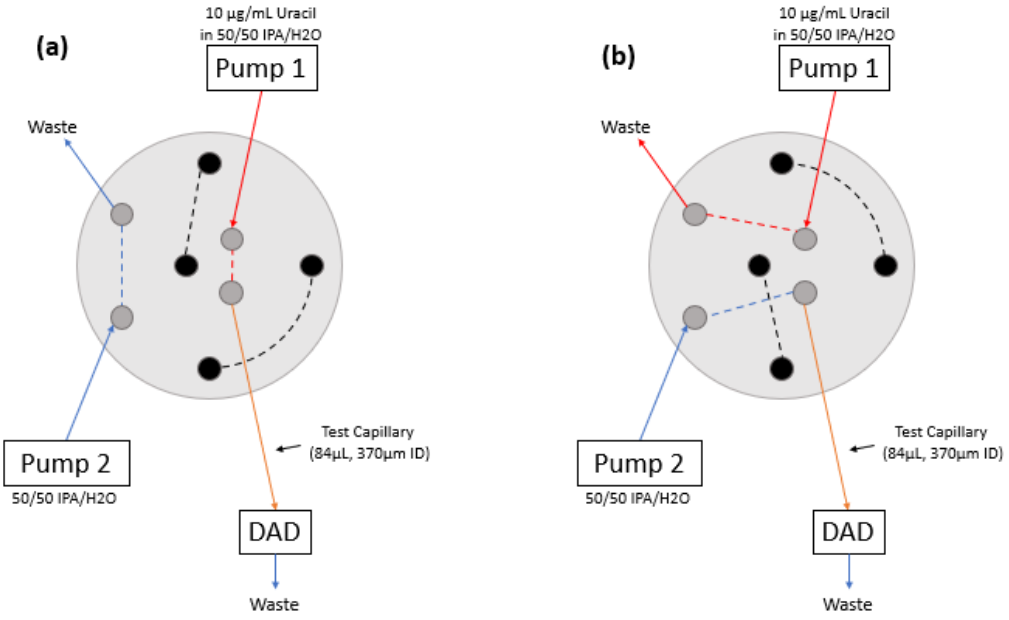

Figure 11. 2D-LC interface scheme used in this work to determine the experimental breakthrough profiles. (a) Valve in filling position, (b) Valve in flush position.

4. Results and discussion

4.1 Simulated concentration profiles

Figure 12a shows the breakthrough profile at the outlet of the loop as a function of time for different loop volumes (V_{loop}=10-320 µL), with fixed flow rates (F_{fill}=0.25mL/min, F_{elu}=2mL/min), and diffusion coefficient $D_{mol}=1x10^{-9}$ m^2/s. Every case was filled with a volume equivalent to half the loop. As it can be observed, the breakthrough time is proportional to the loop volume, and the shape of the curves become broader from left to right, or in other words, as the residence time of the sample inside the loop increases.

To remove the effect of loop volume and compare the shape of these curves, the breakthrough profiles as a function of the dimensionless elution volume V' (see Eq. 19) are illustrated in Figure 12b. It is interesting to note that the tail becomes steeper and shorter with increasing loop volume. As the residence time increases for larger loop volumes, the molecules have more time for radial diffusion and thus to sample the different flow paths across the diameter of the loop, resulting in more symmetrical and less tailing peaks. Moreover, there is a small delay before the elution starts for the largest volume (red curve) that decreases with the loop volume until it disappears for the lowest volume (blue curve), as the amount of species that only experiences the highest velocity in the centre of the loop and thus breakthrough right at the start of the elution step, decreases with increasing filling time or loop volume.

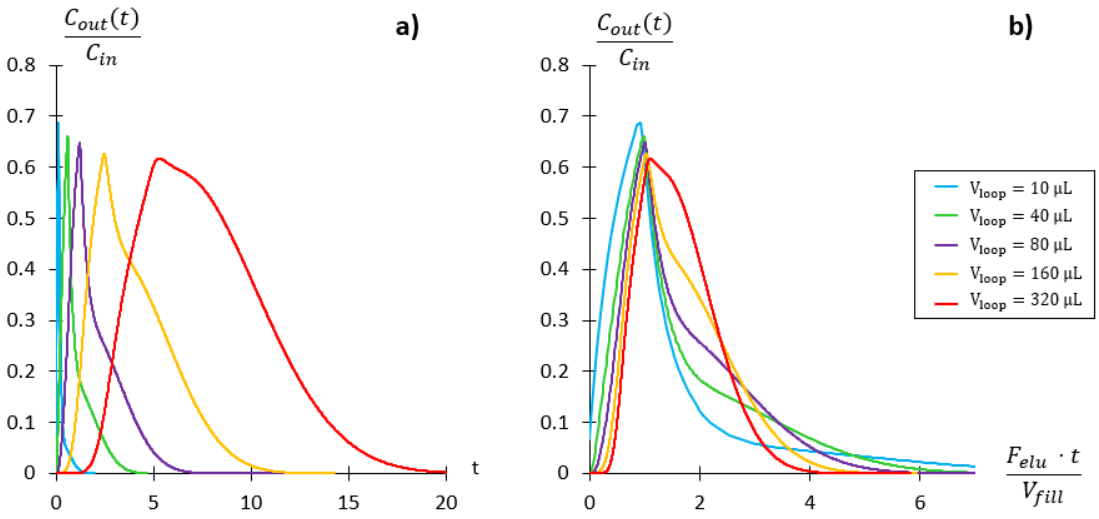

Figure 12. (a) Simulated breakthrough profiles for different loop volumes V_{loop}=10, 40, 80, 160, 320 µL. (b) Similar to (a) but plotted versus dimensionless filling volume. $D_{mol}=1x10^{-9}$ m^2/s , F_{fill}=0.25mL/min, F_{elu}=2mL/min in all cases.

To take into account other parameters including filling/elution flow rates, loop internal diameter and diffusion coefficient, it is more convenient to use the dimensionless elution time t^*_{elu}, previously defined in Eq. 9, since two dimensionless elution profiles will be identical if they have the same t^*_{elu} and ratio of filling and elution flow rates F_{elu}/F_{fill} [3], as it can be seen in Figure 13. This of course reduces the amount of conditions that need to be investigated.

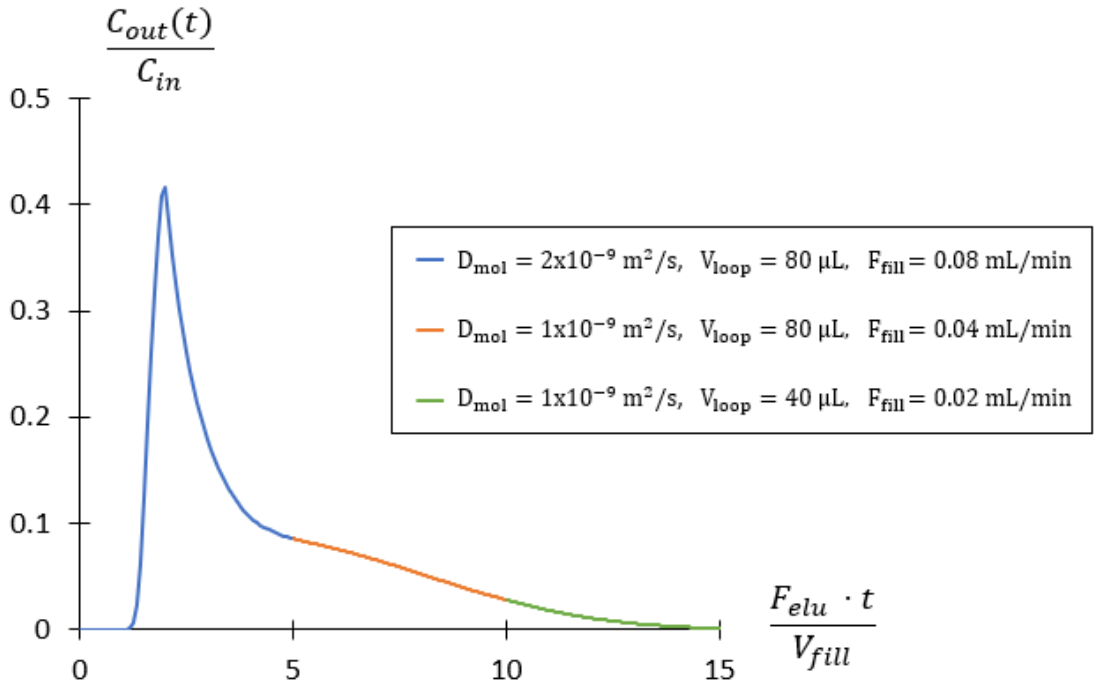

Figure 13. Simulated dimensionless breakthrough profiles in different conditions leading to same value of t^*_{elu}=0.031 and Felu/Ffill=8.

Figure 14 shows the influence of F_{elu}/F_{fill} on the dimensionless breakthrough profiles. A larger F_{elu}/F_{fill} is translated into a lower residence time during elution for a fixed loop volume and F_{fill}, and consequently, the solute has less time to radial equilibrate during elution, leading to larger tails. This is the reason why the elution profiles evolve from a Gaussian shape into a sharper peak with a longer tail one when F_{elu}/F_{fill} increases.

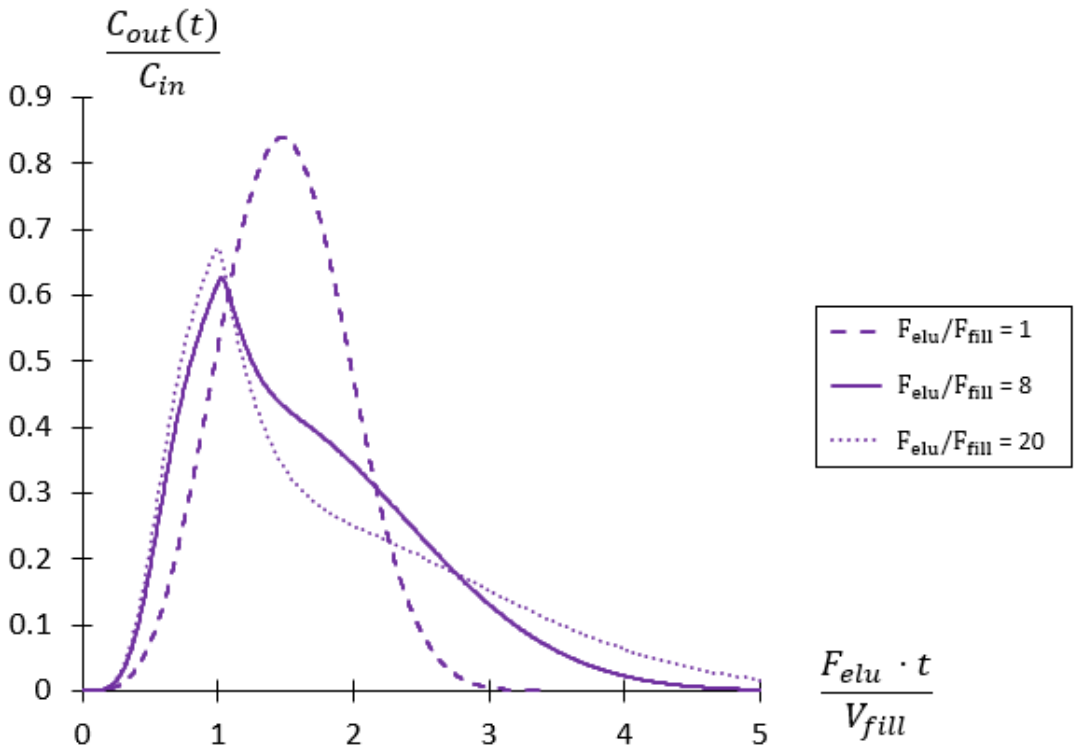

Figure 14. Simulated dimensionless breakthrough profiles for different F_{elu}/F_{fill} with D_{mol}=1x10^{-9} m^2/s , V_{loop}=160 µL and F_{fill}=0.25 mL/min.

The dispersion that occurs inside the sample loop can be measured in terms of the peak width or volumetric variance (σ_V^2), and if the dimensionless elution profiles are overlapping when F_{elu}/F_{fill} and t_{elu}^* are constant, then the volumetric variance will be the same. From Figure 15, it can be seen how the dimensionless volumetric variance vary with t_{elu}^* at different F_{elu}/F_{fill} obtaining a curve that goes through a maximum at very low t_{elu}^* . The volumetric variance has been normalized to V_{fill}^2 to eliminate the effect of loop volume and make the representation entirely dimensionless. The decrease in normalized peak variance at high t_{elu}^*-values for all curves is because this corresponds to conditions where there is sufficient time for radial diffusion to eliminate radial concentration differences due to the parabolic flow profile. Because molecules have time to diffuse away from low velocity region (i.e near the wall due to the no-slip condition) the formation of a large tail in the elution profile is avoided, resulting in more Gaussian like peaks and lower volumetric variance-values are obtained. On the other hand, when t_{elu}^* is very small, two possible hypotheses could explain why σ_V^2/V_{fill}^2 decreases again: the effect of the mass transfer entry length may become more relevant up to a point where the concentration profile does not longer develop a full parabolic (will be discussed in

Section 4.3), or the required value of the concentration cut-off to stop the peak integration (will be discussed in Section 4.4). Regarding the effect of increasing $F_{elu}/F_{fill,}$ it was observed that for small t^*_{elu}-values σ_V^2/V_{fill}^2 is larger for higher F_{elu}/F_{fill} because long shallow tails are formed. Although corresponding to only small concentration (less than 0.5% of the peak maximum), these differences in tailing affects the resulting peak variance significantly. For increasing t^*_{elu}-values, the different curves converge at an intersection point (t^*_{elu}~0.025), from where σ_V^2/V_{fill}^2 is slightly smaller at higher F_{elu}/F_{fill}-ratio, allowing more time for radial diffusion during the filling step. A further explanation for these observations will be given in Section 4.4.

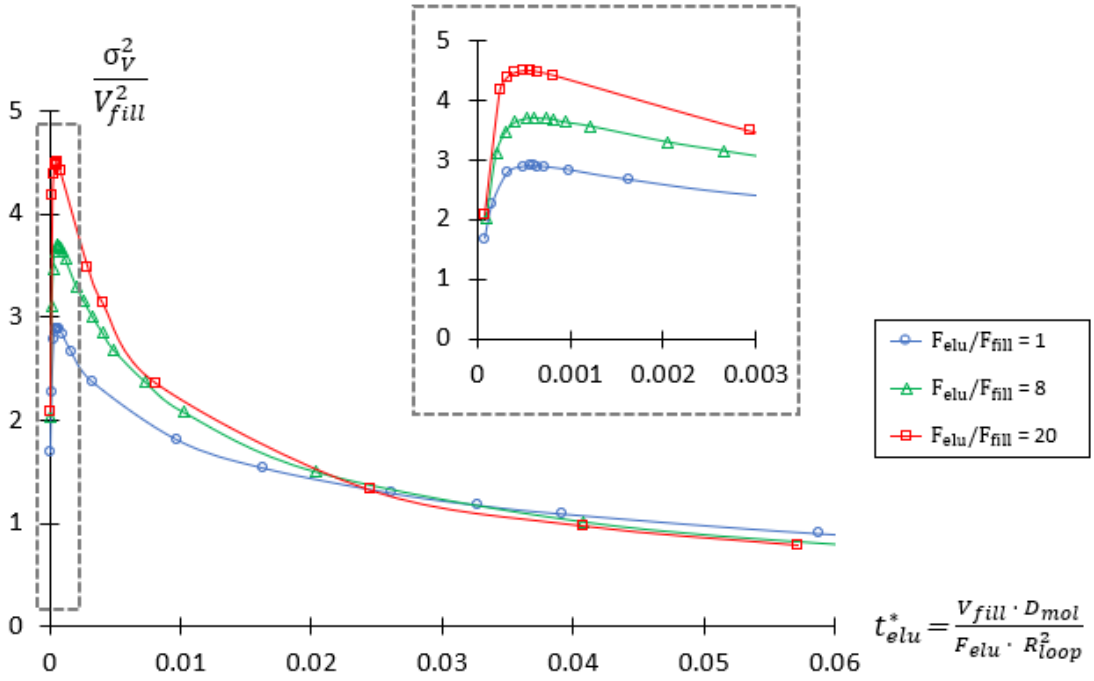

Figure 15. Dimensionless volumetric variance of the elution breakthrough profile versus t^*_{elu} for different F_{elu}/F_{fill}.

A more extensive study of the maximum of σ_V^2/V_{fill}^2 is illustrated in Figure 16, where additional ratios (4, 14, 40 and 80) were investigated. From these dataset, two number of interest where extracted, i.e. the height of the maxima of the curves $(\sigma_V^2/V_{fill}^2)_{max}$ and their position $(t^*_{elu})_{max}$. Firstly, a linear dependency of the maximum σ_V^2/V_{fill}^2 with the square root of F_{elu}/F_{fill} in the investigated range is observed (same trend was observed in FILO experiments carried out by Moussa *et al.* [25]). One hypothesis for this behaviour could be that maximum peak variance are obtained in a region where convective forces are much higher than diffusive, so little radial diffusion

will occur. As consequence, breakthrough profiles with long tailings would be obtained, and peak variance calculated by the method of moments is very sensitive to slight increases in tailing (more details in Section 4.4). Regarding the t^*_{elu}-values at which the maximum σ_V^2/V_{fill}^2 is found, an increasing positive trend with F_{fill}/F_{elu} is found (note that is the inverse of the commonly considered flow rate ratio) that levels off at F_{fill}/F_{elu} and decreases again slightly for the ratio 1. As the behavior is similar to inverse of a typical van Deemter curve observed in chromatography, the inverse of $(t^*_{elu})_{max}$ was fitted according to this equation.

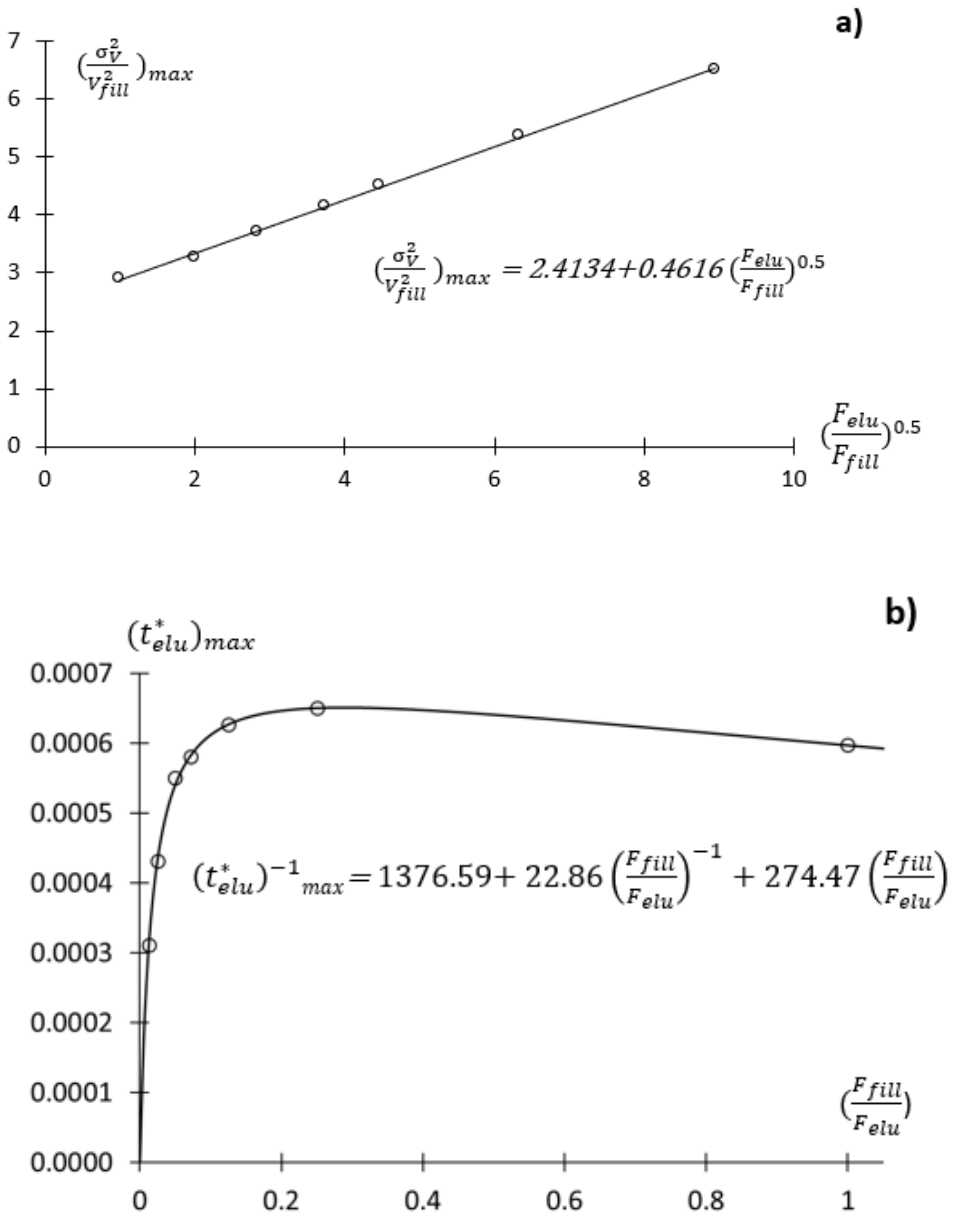

Figure 16. a) Maximum σ_V^2/V_{fill}^2 versus the square root of F_{elu}/F_{fill} for ratios 1, 4, 8, 14, 20, 40 and 80. b) t^*_{elu} at maximum σ_V^2/V_{fill}^2 versus F_{elu}/F_{fill}.

Knowing these fitting functions, it is possible to normalize the curves in Figure 15, in addition the other F_{elu}/F_{fill} simulated for Figure 16, by dividing both axis by their maximum value, yielding:

$$Y = \frac{\sigma_V^2}{V_{fill}^2} / \left(\frac{\sigma_V^2}{V_{fill}^2}\right)_{max} \tag{23}$$

$$X = ln[t_{elu}^*/(t_{elu}^*)_{max}] \tag{24}$$

Figure 17 shows the result of normalizing both axis, showing a good overlap of the curves for different F_{elu}/F_{fill}. The natural logarithm was applied to the x-axis because a Gaussian-like distribution of the values is obtained, which is also centred around zero. The black solid line represents a fitting function, where the fitting parameters were obtained by Least Square Minimization, taking into account all data points available.

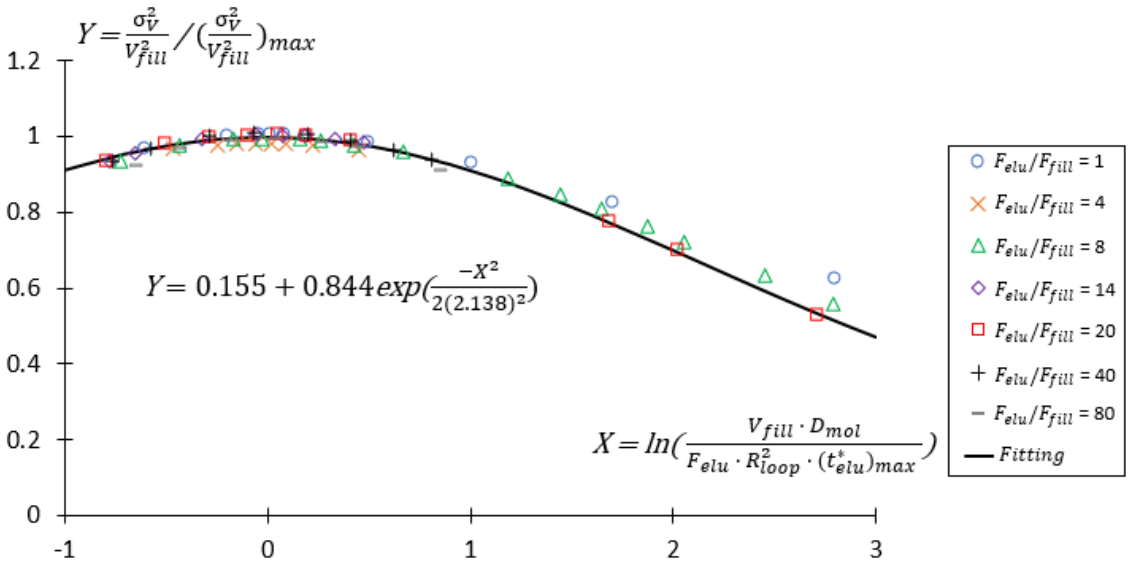

Figure 17. Normalized plot for the different F_{elu}/F_{fill} and a Gaussian-like fitting function.

Therefore, a fitting function was obtained, which combined with Eq.23 and Eq.24, enables the prediction of the peak variance in a F_{elu}/F_{fill} range between 1 and 80, and for any possible value of t_{elu}^* in a straight capillary operated in FIFO mode with a filling fraction of 0.5. Although the Gaussian-like fitting function has been obtained in the normalized domain, the predictions are equally successful in the σ_V^2/V_{fill}^2 versus t_{elu}^* domain, as it is illustrated in Figure 18.

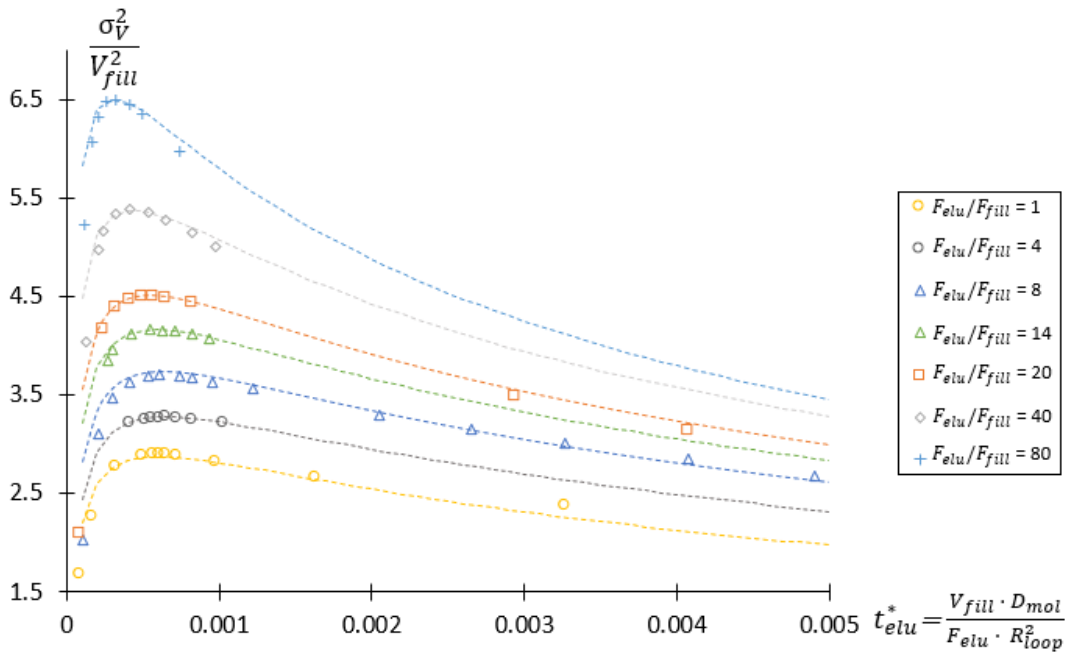

Figure 18. Peak variance predictions using the fitting functions and Eqs. (23)-(24) (dashed line) and simulated data in the σ_V^2/V_{fill}^2 *versus* t^*_{elu} *domain.*

It is important to mention that in FIFO the filling fraction is an important parameter affecting the peak variance, as lower filling fraction means that the same injected peak volume needs to travel a longer distance at F_{elu} (hence more dispersion). On the other hand, a filling fraction over 0.5 results in breakthrough of the sample during filling as the maximum velocity is twice the average velocity yielding a sharper peak front during elution. This is illustrated in Figure 19, where the elution profiles for different filling fractions are displayed. The amount of sample lost as a function of the filling fraction for a fixed t^*_{elu} is summarized in Table 2. As expected, no sample is lost for a filling fraction of 50% or lower. The amount of sample lost decrease with increasing $F_{elu}/F_{fill,}$ as for higher F_{elu}/F_{fill}, the loop is filled at a lower flow rate, allowing more time for radial diffusion and thus reducing the amount of solutes that only experienced the thigh flow rates in the middle of the sample loop.

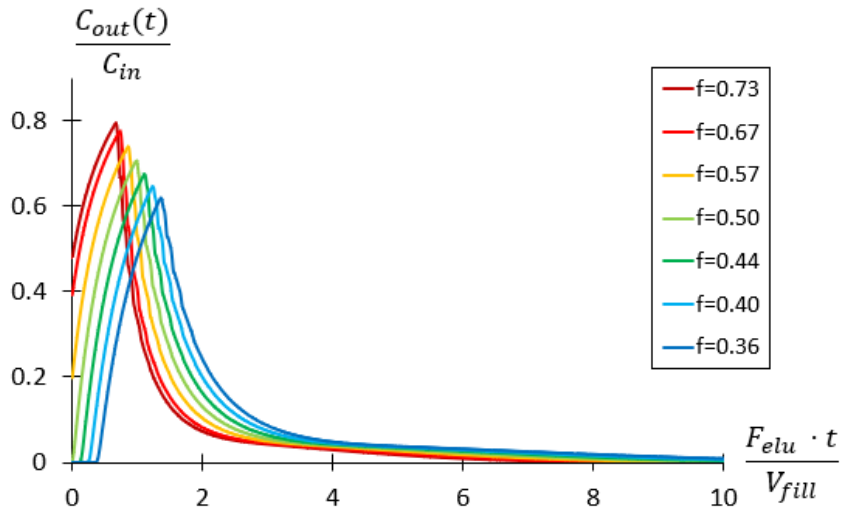

Figure 19. Simulated breakthrough profiles for different filling fraction, with F_{elu}/F_{fill} = 8 and t^*_{elu}=0.0041.

Table 2. Sample loss for different filling fractions and F_{elu}/F_{fill}, with t^*_{elu}=0.0041.

	Sample loss (%)		
Filling fraction	**F_{elu}/F_{fill} = 1**	**F_{elu}/F_{fill} = 8**	**F_{elu}/F_{fill} = 20**
0.73	9.27	8.74	7.51
0.67	5.75	5.44	4.52
0.57	1.14	1.17	0.85
0.50	0	0	0
0.44	0	0	0
0.40	0	0	0
0.36	0	0	0

Figure 20 shows how σ_V^2/V_{fill}^2 increases linearly with inverse square of filling fraction. Therefore, if filling fraction is not exactly 0.5, the resulting peak variance is strongly affected and the obtained model will no longer be an accurate prediction. This is important for the evaluation of the experimental measurements, as technical limitations in the experimental set-up do not always allows to perfectly achieve a 50% loop filling.

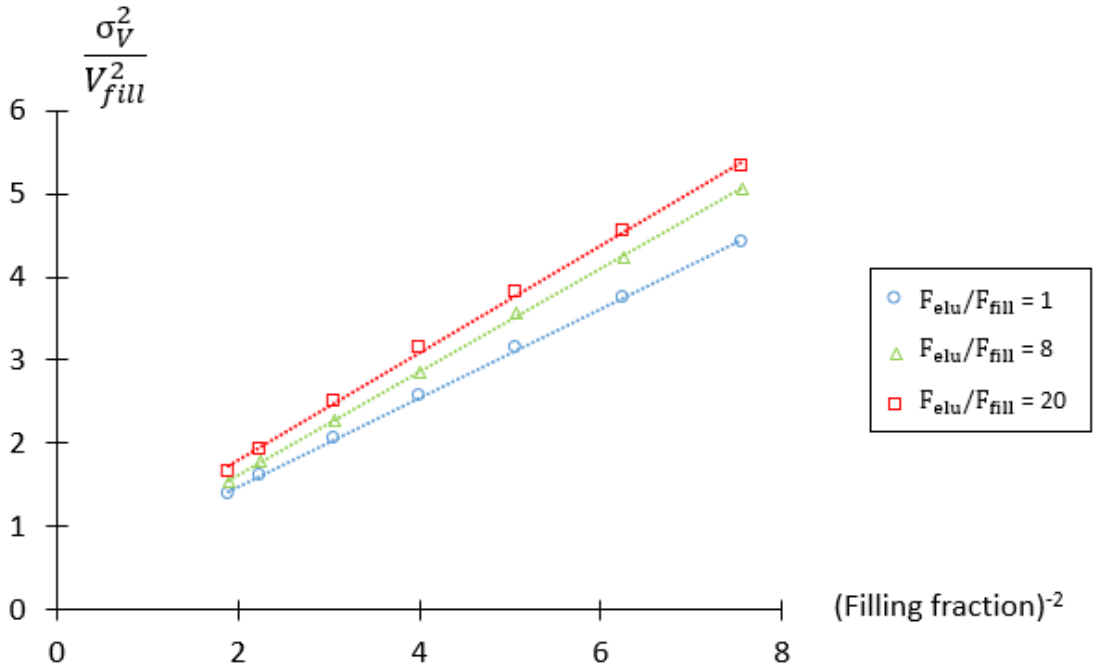

Figure 20. Peak variance versus inverse of filling fraction for F_{elu}/F_{fill} = 1,8,20, and t^*_{elu}=0.0041.

4.2 Comparison of simulated and experimental results

A series experimental measurements were performed to verity the numerical results obtained from the CFD simulations. These experiments were carried out by Prof. Dwight Stoll's group at Gustavus Adolphus College (Minnesota USA) using a setup described in Section 3.2. In Figure 21-23 are compared the numerical results (grey squares), previously plotted in Figure 15, are compared with the experimental results obtained in a straight capillary (orange circles) and in a coiled one (blue triangles). The experimental results from the straight capillary setup show a similar behaviour to the numerical data in F_{elu}/F_{fill}=8 and 20, although the peak variance is always a little bit higher. This might be because in experimental measurements there are some contributions to band broadening (i.e. connections, valve, detector) that are not included in the simulations.

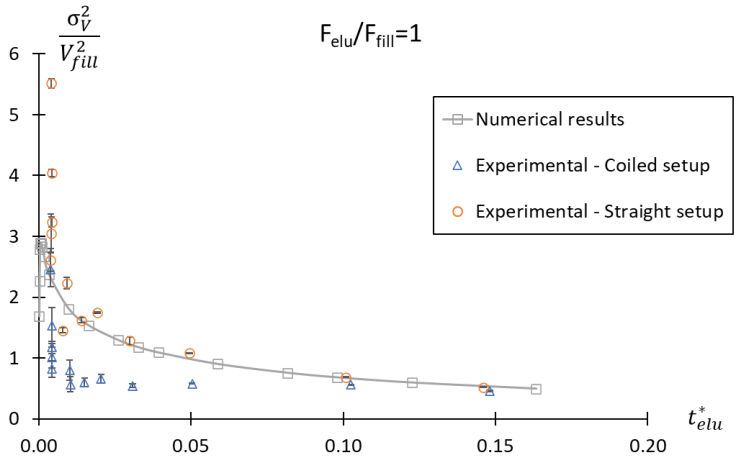

Figure 21. Comparison between experimental results (in coiled and straight setup) and numerical results from CFD simulations in the σ_V^2/V_{fill}^2 *versus* t^*_{elu} *domain for* F_{elu}/F_{fill}=1

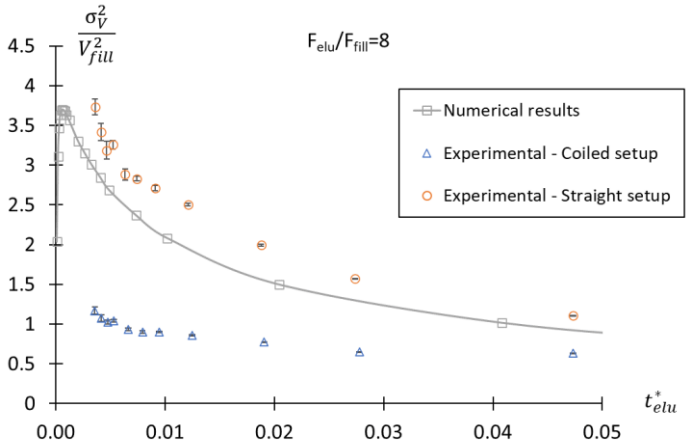

Figure 22. Comparison between experimental results (in coiled and straight setup) and numerical results from CFD simulations in the σ_V^2/V_{fill}^2 *versus* t^*_{elu} *domain for* F_{elu}/F_{fill}=8

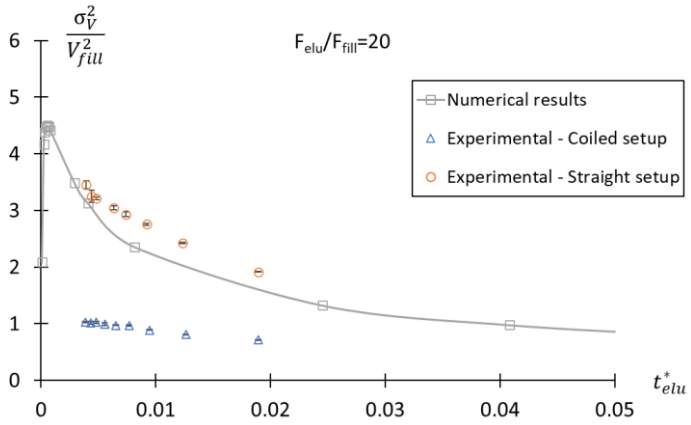

Figure 23. Comparison between experimental results (in coiled and straight setup) and numerical results from CFD simulations in the σ_V^2/V_{fill}^2 *versus* t^*_{elu} *domain for* F_{elu}/F_{fill}=20

When looking at the experimental results obtained in a coiled setup, secondary flow effects due to centripetal forces are enhancing the radial dispersion of the solute, in other words, the system behaves as if the species has a higher D_{mol}, and these effects are more relevant as the flow rate increases (i.e. in the lower t^*_{elu} range). For cases where $F_{elu}/F_{fill} > 1$, this enhanced radial dispersion is more significant during elution than during filling step as $F_{elu} > F_{fill}$. In that case, the ratio F_{elu}/F_{fill} should in fact be replaced by t^*_{fill}/t^*_{elu}, where each t^*should be recalculated with the actual radial dispersion coefficient D_{rad} as in Eq. (25).

$$\frac{t^*_{fill}}{t^*_{elu}} = \frac{F_{elu} \cdot D_{rad,fill}}{F_{fill} \cdot D_{rad,elu}} \tag{25}$$

However, the only way to estimate D_{rad} is from experimental results for $F_{elu}/F_{fill}=1$, as here only parameters needs to be estimated (since $D_{rad,elu} = D_{rad,fill}$), whereas for $F_{elu}/F_{fill} \neq 1$ both the $D_{rad,elu}$ and $D_{rad,fill}$ need to be estimate. Unfortunately, the dataset for $F_{elu}/F_{fill}=1$ shows rather high scatter (see Figure 21), and the accuracy of the injected volumes was rather low (see below), so it would be required to repeat these measurements under conditions where these parameters can be better controlled, to estimate the values of D_{rad} as a function of flow rate.

In $F_{elu}/F_{fill}=1$ a significant scatter in the experimental data can clearly observed. The reason of this dispersive tendency is the time step controller during the filling step, which is not accurate enough to get the desired filling volumes with the high F_{fill} required to obtain sufficiently low enough t^*_{elu}. Figure 24 shows the actual loop filling fraction reached in the experimental conditions at different F_{elu}/F_{fill}, where is clearly observed that for F_{elu}/F_{fill} =1 the filling fraction is not constant anymore, and as it was previously explained, the filling fraction is an important parameter affecting the peak variance in FIFO mode. In addition, it can be observed that for $F_{elu}/F_{fill}=8$ and $F_{elu}/F_{fill}=20$, loop filling fractions slightly below 0.5 are found, which also explains why the experimental data is slightly above the predicted values from the numerical model.

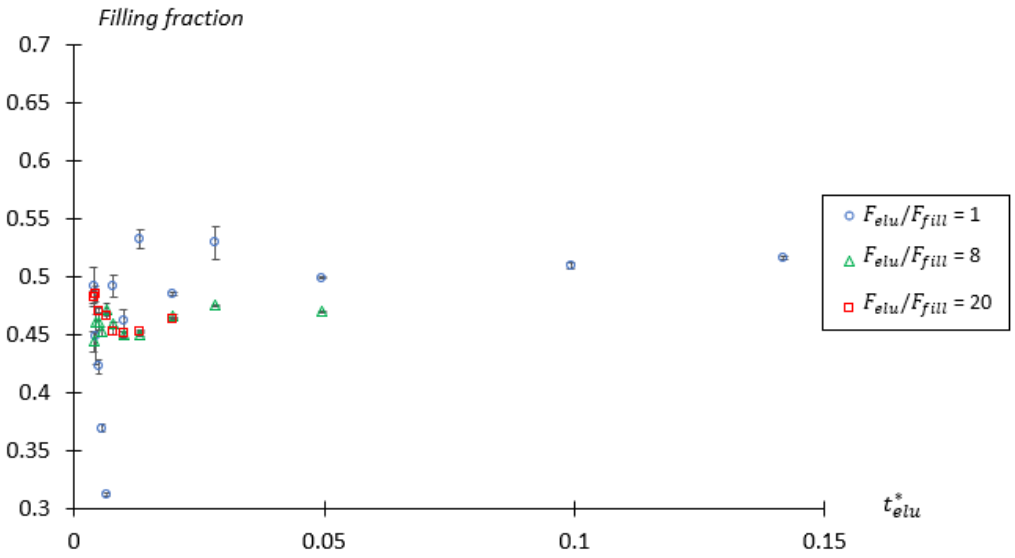

Figure 24. Filling fraction measured from experimental data in straight capillary versus t^*_{elu} for different F_{elu}/F_{fill}

This data can also be used to confirm the effect of filling fraction on the peak variance shown for the numerical results in Figure 20. Figure 25 displays the deviation in σ_V^2/V_{fill}^2 of the experimental data obtained in the straight setup respect the numerical data from simulations versus the inverse square of the filling fraction, demonstrating same trend as was found for the numerical simulations.

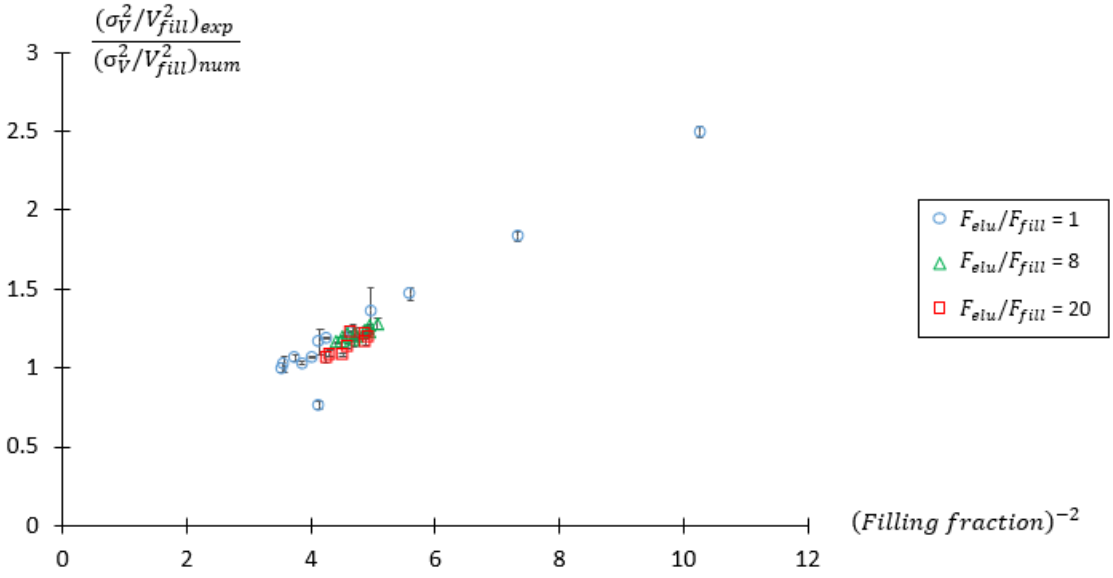

Figure 25. Deviation in peak variance of experimental data respect numerical results versus inverse square of filling fraction in straight capillary for different F_{elu}/F_{fill}.

As can be seen in Figs. 21-23, it was not possible to investigate smaller t^*_{elu}-values as this corresponded to impractical experimental conditions that are in addition not relevant in practice. Unfortunately, this also did not allow to measure conditions near the observed maximum in simulations. One possibility is to use a shorter and broader sample loop in future experiments.

4.3 Determination of the entry length

In Section 4.1, the importance of the entry length was mentioned, specially at low t^*_{elu}-values that correspond to a region where the convective forces due to the flow rate are much higher than the radial diffusion. Table 3 shows the theorical hydrodynamic entry length calculated with Eq.11 within the F_{fill} range used in the simulations. The loop volume used in most of the simulations was V_{loop}=80 μL, corresponding to a length of the loop L_{loop}=0.832 m. Therefore, even in the worst scenario, the flow becomes fully developed before it reaches the 0.25% of the L_{loop}.

Table 3. Theorical hydrodynamic entry length at different F_{fill}.

F_{fill} (ml/min)	Re	Entry length (m)
2.00	120.68	2.11E-03
0.96	57.93	1.01E-03
0.48	28.96	5.07E-04
0.24	14.48	2.53E-04
0.16	9.65	1.69E-04
0.12	7.24	1.27E-04
0.10	5.79	1.01E-04
0.08	4.83	8.45E-05
0.07	4.14	7.24E-05
0.06	3.62	6.34E-05

To verify the hydrodynamical entry length values based on Reynolds number, some simulations were performed where the axial velocity was monitored along the centre of the capillary. Figure 26 shows the velocity along the central axis, normalized to the velocity when the flow is fully developed in each case, versus the length normalized to the injection length (V_{loop}/2 since the filling fraction was 0.5). As it is expected, the

higher the filling flow rate used, the larger the length where the flow becomes fully developed.

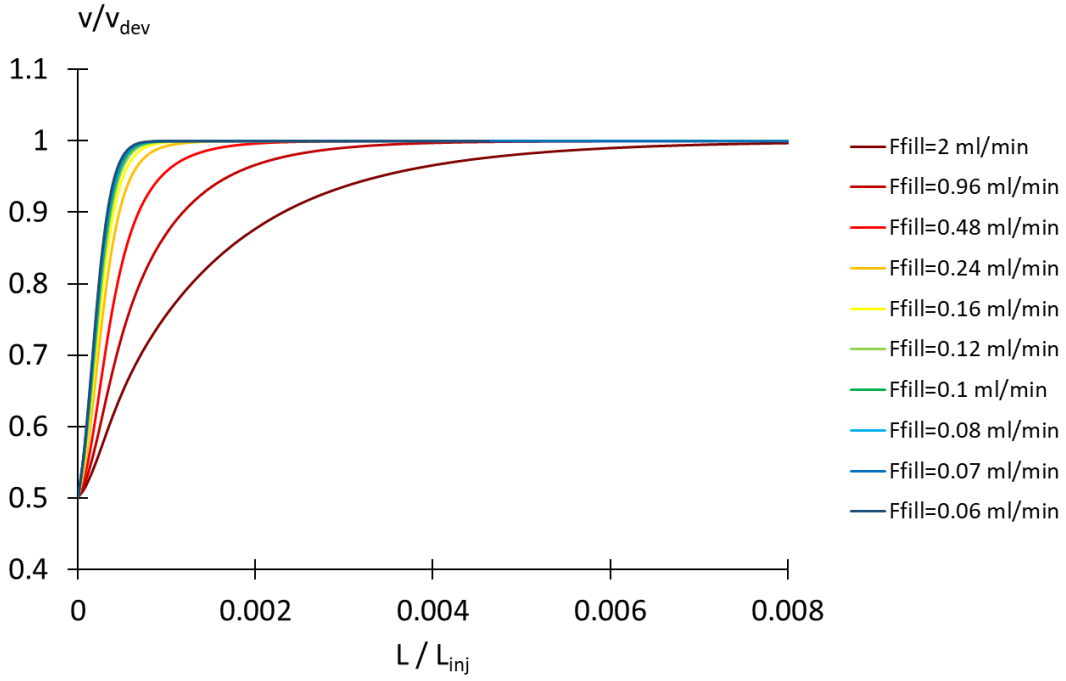

Figure 26. Normalized velocity along the axis versus length.

From the simulations, it is possible to obtain the exact length at which the 98% of the length needed by the flow to become fully developed. In Figure 27 can be appreciated the comparison of the numerical and theorical entry, resulting in a good agreement.

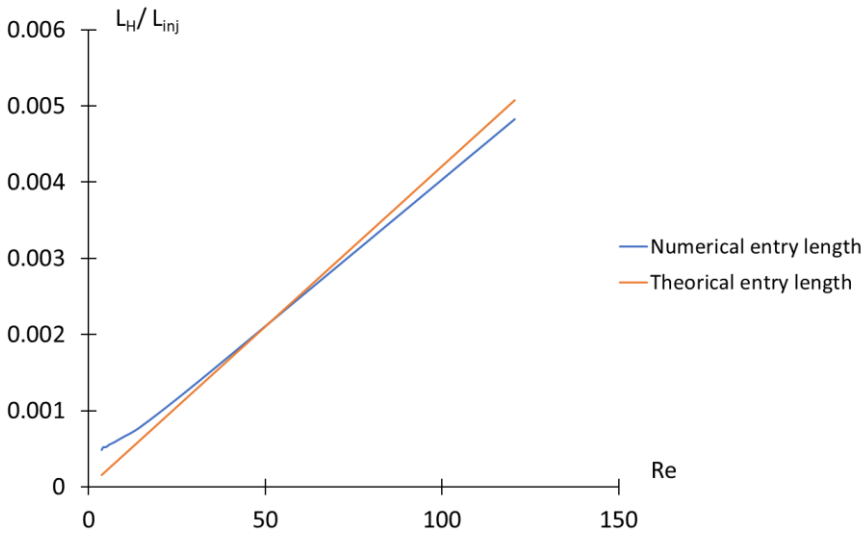

Figure 27. Hydrodynamical entry length normalized to the injection length versus the Reynolds number.

To determine whether the hydrodynamical entry length has an effect on peak variance or not, some simulations were performed by using periodic boundary conditions. For this condition, the inlet and outlet of the loop will be treated as if they were physically connected, so the flow behaves like in bulk. In Figure 28 are compared the results from simulations without hydrodynamical entry length effect and the previous ones, resulting in only a minor increase in peak variance. Therefore, it can be concluded that the hydrodynamical entry length is not the cause of the small peak variances at low t^*_{elu}-values.

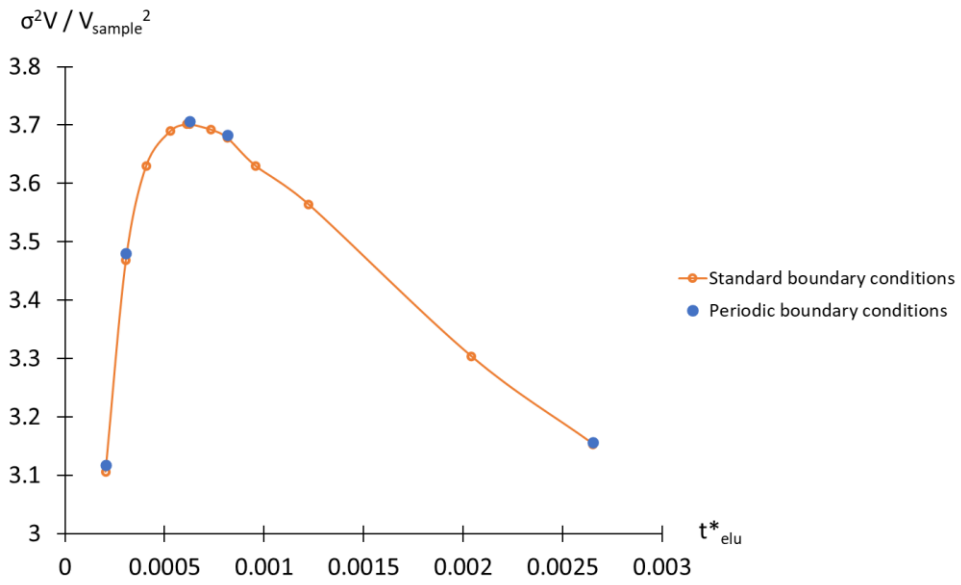

Figure 28. Effect of the hydrodynamical entry length on the normalized peak variance at different t^*_{elu}.

Afterwards, the mass transfer entry length is analysed. Table 4 shows the mass transfer entry length estimated by using Eq. 17 for some conditions before, near and after the maximum σ_V^2/V_{fill}^2 with F_{elu}/F_{fill}=8 and V_{loop}=80 µL. This time, the mass transfer entry length is significant when compared to the L_{loop}, specially at low t^*_{fill} as it is expected. In fact, only for t^*_{fill} = 0.327 the entrance length is shorter than the loop length for V_{loop} = 80 µL

Table 4. Mass transfer entry length for different t^*_{fill}-values with $F_{elu}/F_{fill}=8$

F_{fill} (ml/min)	t^*_{fill}	MT length (m)
0.48	0.003	25.465
0.24	0.007	12.732
0.48	0.016	5.093
0.48	0.082	1.019
0.24	0.327	0.255

To determine the mass transfer entry length with numerical simulations, the zero normal gradient on the wall was replaced by a fix mass fraction. Figure 26 illustrates the effect of t^*_{fill} the mass transfer entry length for a V_{loop}=80 µL. Being the loop length L_{loop}=3.741 m, only the two highest t^*_{fill}seems to get a fully developed concentration profile, while in the other simulations the profile is still developing.

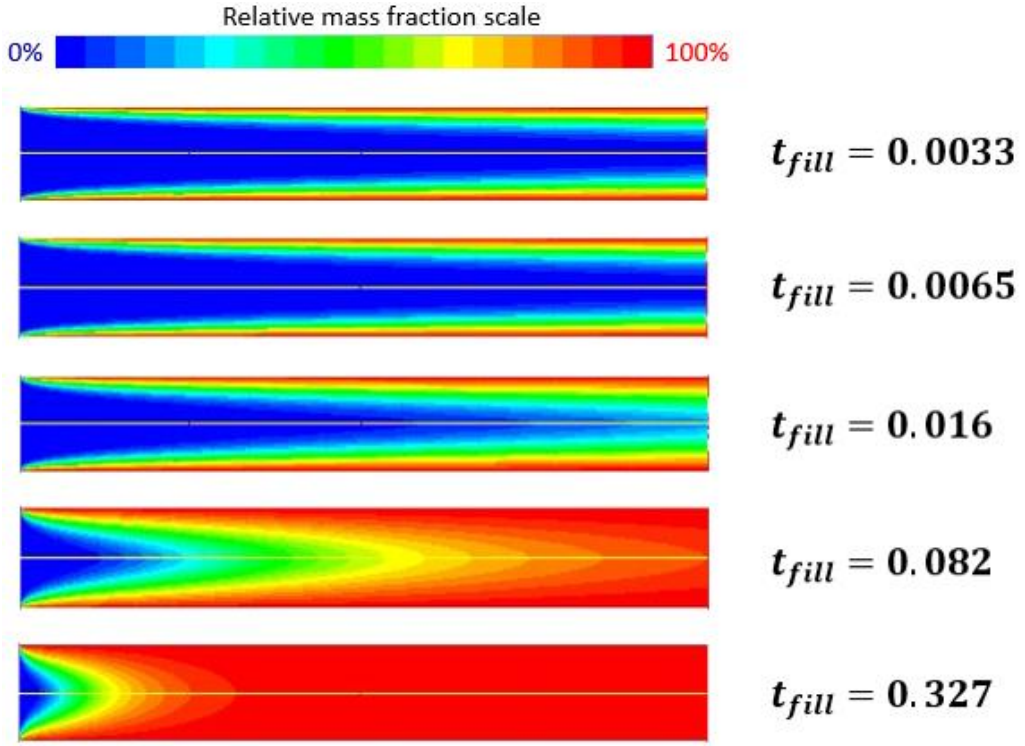

Figure 29. Steady-state simulated species profiles with a fix mass fraction at wall. F_{fill}=0.24-0.48 ml/min, V_{loop}=360 µL, the length has been adjusted by a scaling factor of 1/1000.

By definition, the mass transfer entry length is the location where the relative concentration profile is constant along the axis:

$$\frac{\partial}{\partial x}\left(\frac{C(r)-C_{center}}{C_{wall}-C_{center}}\right)\rightarrow 0 \qquad (25)$$

Therefore, the species distribution monitor planes can be analysed at different positions in the loop to obtain the radial concentration profile along the axis. In Figures 30-34 the relative concentration in the radial direction at different loop lengths is plotted for different t^*_{fill}-values. From Eq. 25, the mass transfer entry length is found when the radial concentration profiles start to overlap. Then, with t^*_{fill} = 0.327 the L_{MT} is between 20 and 30cm, and with t^*_{fill} = 0.082 is between 100 and 120cm, whereas for lower t^*_{elu} simulations the L_{MT} is larger than the loop length. These results agree with the theorical predictions in Table 4.

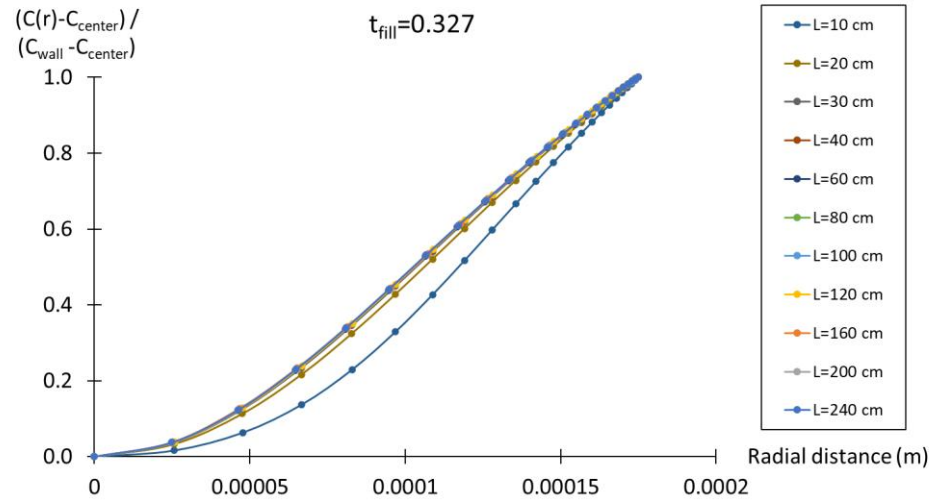

Figure 30. Relative concentration in the radial direction at different loop lengths with t^*_{fill}=0.327.

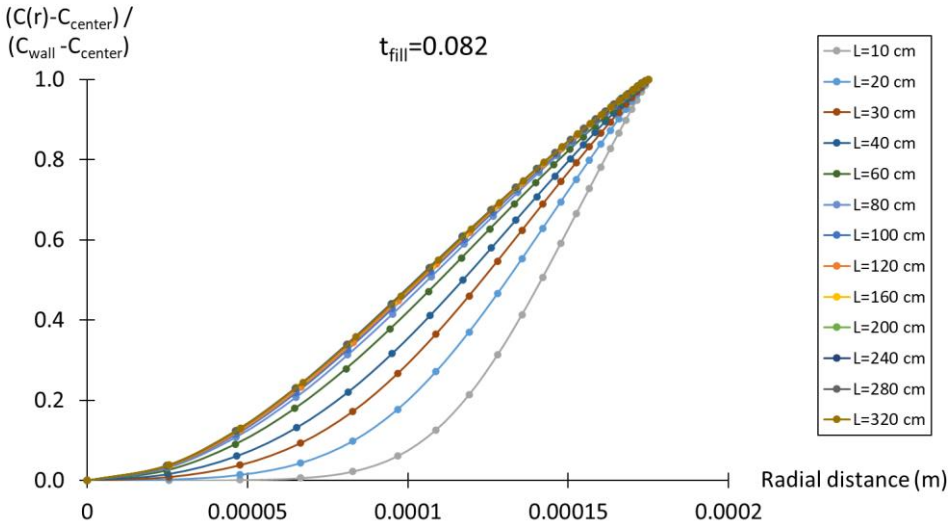

Figure 31. Relative concentration in the radial direction at different loop lengths with t^*_{fill}=0.082.

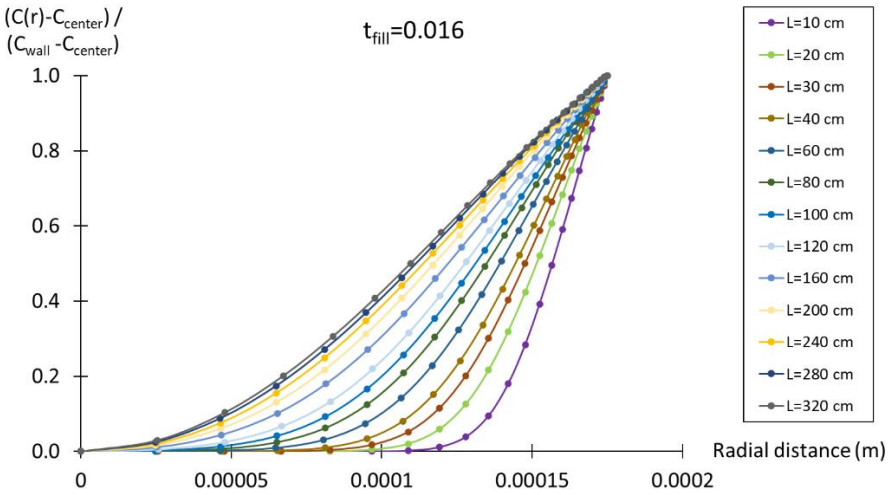

Figure 32. Relative concentration in the radial direction at different loop lengths with t^*_{fill}=0.016.

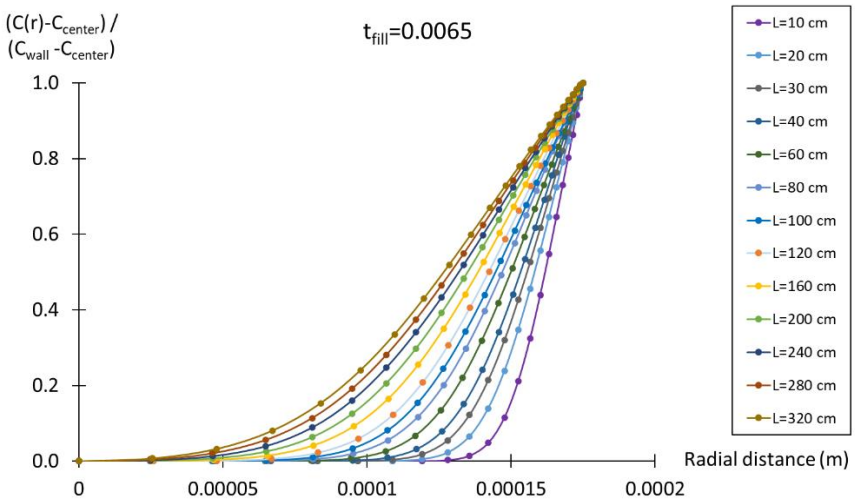

Figure 33. Relative concentration in the radial direction at different loop lengths with t^*_{fill}=0.0065.

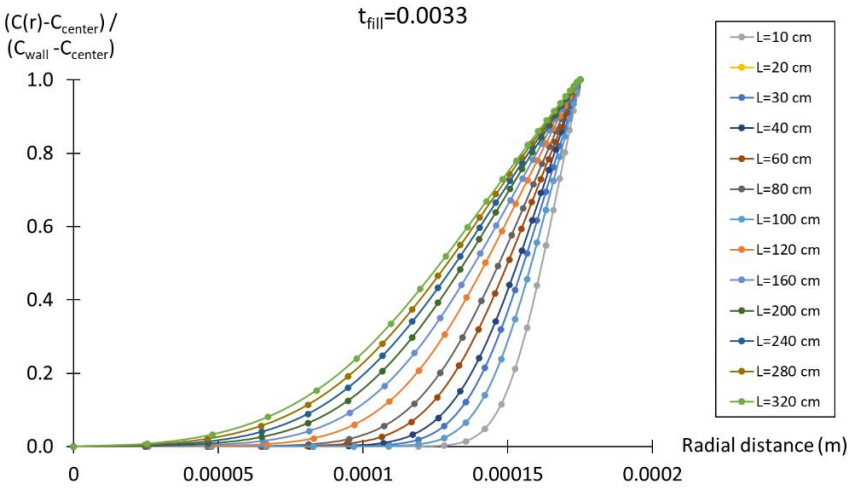

Figure 34. Relative concentration in the radial direction at different loop lengths with t^*_{fill}=0.0033.

Finally, it can be concluded that the mass transfer entry length might have a significant influence on the peak variance, especially at low t^*_{elu}-values, whereas the hydrodynamic entry length has little to no effect. The effect of this entrance length becomes clear when comparing the elution profiles for decreasing t^*_{elu}-values (see e.g. Figure 40 further on), where the peaks evolve from a Gaussian like profiles towards much more sharp and tailing profiles as the effect of the L_{MT} becomes more prominent.

4.4 Effect of F_{elu}/F_{fill} ratio

Previously on Section 4.1, a larger peak variance was observerd for higher F_{elu}/F_{fill} values at low t^*_{elu}, whereas opposite trend was obtained for large t^*_{elu}-values (see Figure 15). In addition, a local maximum in peak variance was observed. To understand the influence of F_{elu}/F_{fill} for different t^*_{elu} values, Figure 35 shows 2D concentration profile plots after the filling step. For a larger F_{elu}/F_{fill} ratio, at a constant t^*_{elu}, the value of F_{fill} is lower. For t^*_{elu}= 0.04 it is clear that as as F_{fill} decreases (i.e. for higher F_{elu}/F_{fill}), the profile changes from an elongated parabolic shape towards a more rectangular plug. As t^*_{elu} decreases, the radial diffusion however becomes less important compared to convection (i.e. lower D_{mol}-value or higher F_{elu}) up to a point where 2D plots are almost identical for t^*_{elu}= 0.0003.

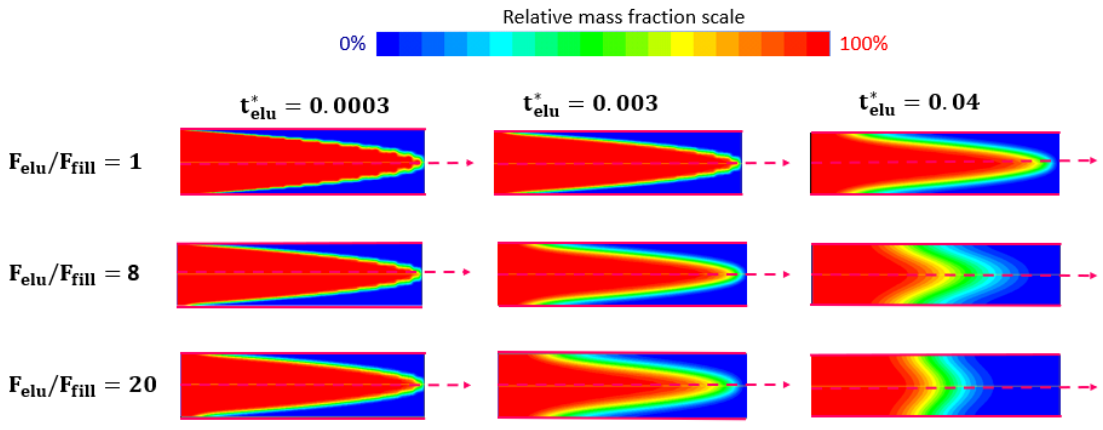

Figure 35. 2D simulated species profiles after filling step, for different t^*_{elu} and F_{elu}/F_{fill} with V_{loop}=80 µL and filling fraction=0.5.

In addition, for F_{elu}/F_{fill} =20 it is clear in Figure 35 that more of the solute reaches the low velocity region near the wall, which can lead to a more extensive tails in the elution

profiles. After analysing the filling step, in Figures 36-38 are displayed: a) the corresponding elution profiles in main axis and peak variances in secondary axis versus V', and b) a zoom on the tailing of the peaks. The former plots in fact present how much of the variance results from which part of the peaks and additionally indicates how much of the full peak variance is considered, i.e. when the integration would not be cut-off at 0.1% of the feed concentration but continued until infinity. For t^*_{elu}= 0.0003, the elution profiles appear to be completely overlapped, but slight tailing differences as presented in Figure 36b affects the final peak variances significantly. As previously mentioned, in this case, a larger F_{elu}/F_{fill} results in more of the sample to be able to reach the wall regions relative to the lower F_{elu}/F_{fill} ratio, hence the tails will be more pronounced resulting in a higher peak variance. This sensitivity using the method of moments is because σ_V^2 changes with the square of the distance to the mean retention time of the peak, so concentration signals further away from the peak centre will increase significantly more than near the peak centre [26]. As t^*_{elu} increases, less tailing is observed in elution profiles due to radial diffusion, and as result the differences in peak variances become smaller. For t^*_{elu}=0.04, the differences in peak variance are the result of the different concentration profiles after the filling step (see also Figure 35). An elongated parabolic shape profile will start eluting earlier than a more rectangular shape profile, and fronting can be observed for F_{elu}/F_{fill} = 1, which increases peak variance. This explains why we observe in Figure 15 higher peak variances for F_{elu}/F_{fill} = 1 for t^*_{elu}≥0.025.

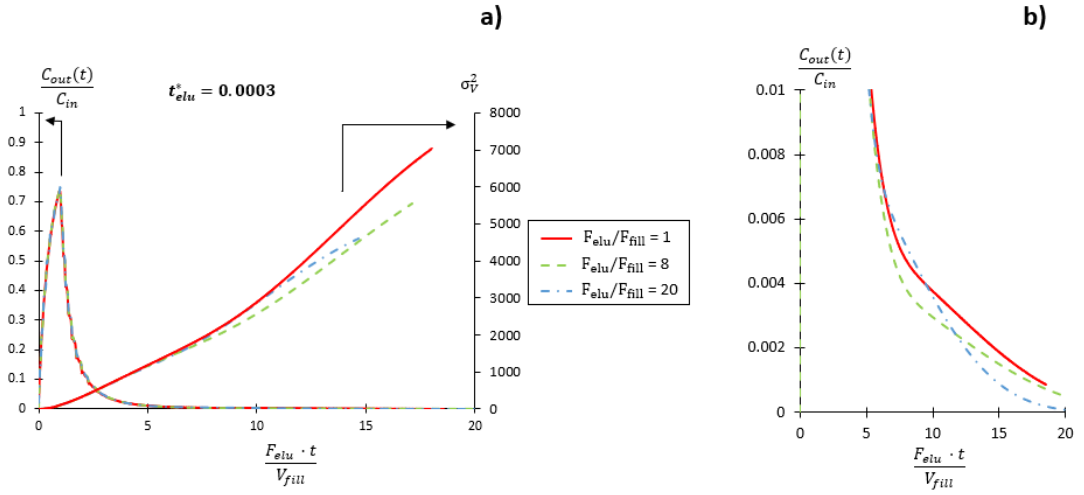

Figure 36. a) Dimensionless breakthrough profiles and peak variance versus V' for t^*_{elu} = 0.0003 and different F_{elu}/F_{fill}. b) Zoom on tailing of breakthrough profiles.

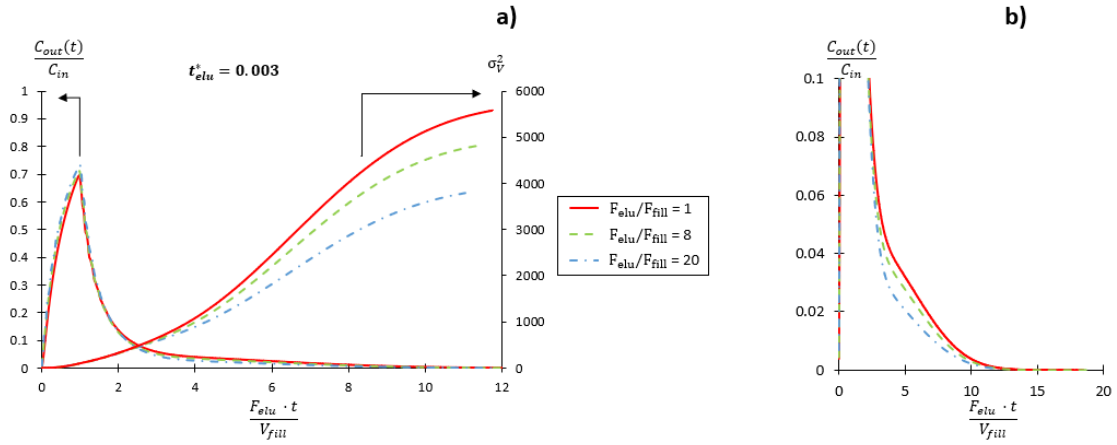

Figure 37. a) Dimensionless breakthrough profiles and peak variance versus V' for $t^*_{elu} = 0.003$ and different F_{elu}/F_{fill}. b) Zoom on tailing of breakthrough profiles.

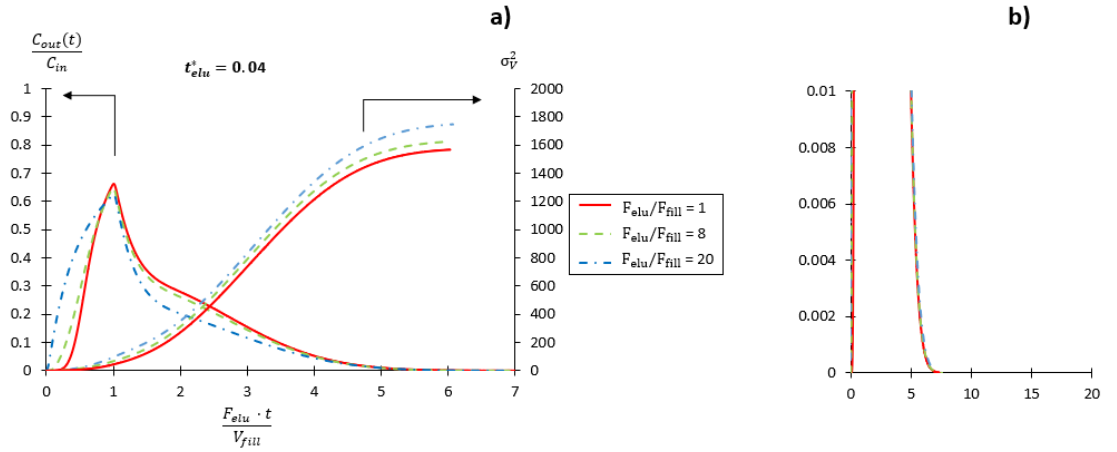

Figure 38. a) Dimensionless breakthrough profiles and peak variance versus V' for $t^*_{elu} = 0.04$ and different F_{elu}/F_{fill}. b) Zoom on tailing of breakthrough profiles.

In addition, it was noticed that for low t^*_{elu}-values, the point where tailing starts is situated at a lower C/C$_{in}$. Figure 39 shows some dimensionless breakthrough profiles for different t^*_{elu}-values and its peak variance. The arrows point where the tail starts. As it can be observed, the tails not only start nearer the cut off value as t^*_{elu} decreases, they are also longer, meaning that an important contribution to band broadening is not considered because a part of the tail is below the cut-off value. This could be the of reason of why a maximum in peak variance is observed in Figure 15, together with mass transfer entry length effect. However, a cut-off = 0.1% was selected because this criterium is feasible in evaluate experimental peaks, where signal can still be distinguished from the noise. In addition, when these low concentration tails are injected from the sample loop into the second dimension column in an actual 2D-LC experiments, they will further be diluted

and certainly fall under the limit of detection. The choose of the most suitable cut-off value or criteria is however not straightforward, as other considerations, such as quantification, can play a role.

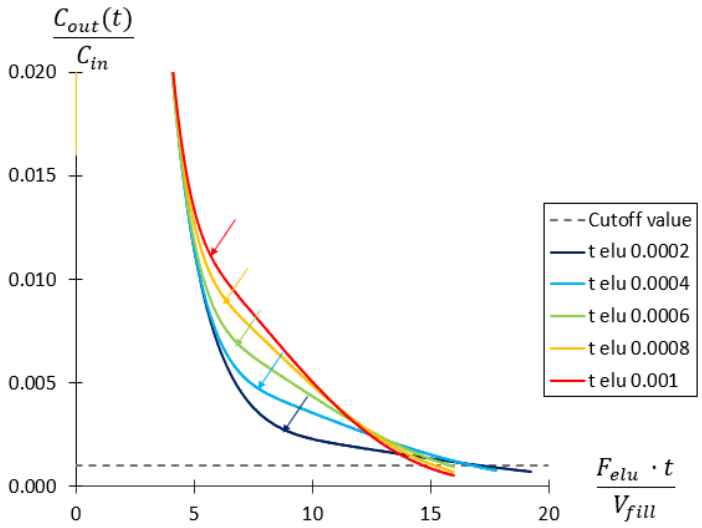

t^*_{elu}	σ^2_V / V^2_{fill}
0.0002	3.11
0.0004	3.63
0.0006	3.70
0.0008	3.68
0.0010	3.63

Figure 39. Zoom on the tails of some breakthrough profiles for F_{elu}/F_{fill} = 8, and a table with the corresponding peak variances.

In conclusion, it has been demonstrated that peak variance increases with F_{elu}/F_{fill} for low t^*_{elu}-values due to slight differences in tailing of the breakthrough profiles, whereas at larger t^*_{elu}-values peak variance decreases with F_{elu}/F_{fill}, since radial diffusion during filling step makes the elution start at different times and causes fronting. It was also found that cut-off criterium might explain why the curves in Figure 15 have a maximum peak variance.

4.5 Mathematical modelling

In this section, we try to improve the mathematical model used to describe LC injection profiles in [21] and [4] (see Eq 10) by making all parameters dimensionless and only dependent on t^*_{elu}, instead of V_{loop} and flow rate in the literature references. In addition, a wide range of t^*_{elu} is investigated. Nondimensionalization is pretty straightforward, and is achieved dividing by the filling volume V_{fill}:

$$V' = \frac{V}{V_{fill}} \tag{26}$$

$$\sigma' = \frac{\sigma}{V_{fill}} \tag{27}$$

$$\tau' = \frac{\tau}{V_{fill}} \tag{28}$$

$$V_0' = \frac{V_0}{V_{fill}} \tag{29}$$

Substituting Eq. 26-29 in Eq. 10 the dimensionless form of the model is obtained, since the other parameters (A, θ) are already dimensionless:

$$h(V') = \frac{A}{2} \cdot \left[\operatorname{erf}\left(\frac{2V' - 2V_0' + V_0'\theta}{\sqrt{2}\sigma'} \right) + \operatorname{erf}\left(\frac{2V_0' - 2V' + V_0'\theta}{\sqrt{2}\sigma'} \right) + \exp\left(\frac{\sigma'^2}{2\tau'^2} + \frac{2V' - 2V_0' + V_0'\theta}{\sqrt{2}\sigma'} \right) erfc\left(\frac{\sigma'^2 - 2V'\tau' + 2V_0'\tau' + \theta V_0'\tau'}{\sqrt{2}\sigma'\tau'} \right) \right] \tag{30}$$

Figure 40 shows all simulated peaks used to obtain the parameters from Eq. 30. The fitting process was performed in Matlab using the lsqnonlin function in the Optimization Toolbox according to [4], where the value of parameter A was constrained to ±0.2% of the maximum value.

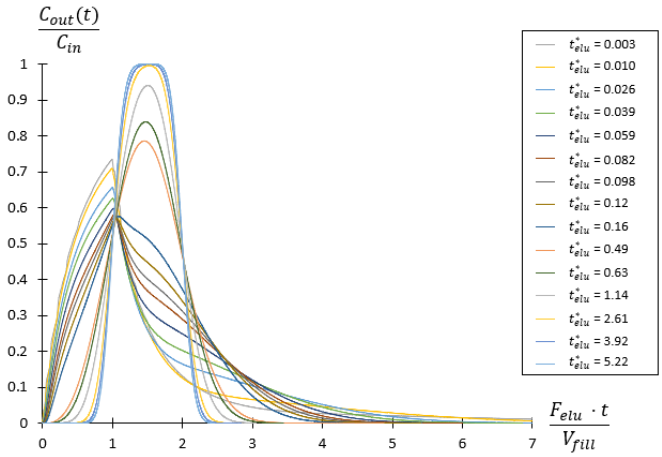

Figure 40. Simulated peaks at different t^*_{elu} and $F_{elu}/F_{fill}=1$ used to obtain the fitting parameters.

Although the model has been studied on simulated peak obtained in the range between t^*_{elu}= 0.003 and t^*_{elu}= 5.224, the mathematical model from Eq. 29 is only able to reproduce the simulated peaks from t^*_{elu}=0.012 on, because below this value long tailings appear that make the model no longer fits simulated profiles. In Wheatherbee *et al.* [4], the model was originally developed for t^*_{elu}= 0.012-2.05, but in a coiled setup that enhances radial dispersion, resulting in more Gaussian shape peaks, so their model is not universal. Moreover, they filled the loops to 80% their volume, meaning that a significant part of the sample is lost because it starts eluting during filling step.

In Figure 41 are displayed the empirical parameters together with the simulated dots in the t^*_{elu} range mentioned, resulting in a good match. It is not surprising the trend followed by σ' versus t^*_{elu} , since peak width decreases for larger t^*_{elu}-values as it is shown in Figure 15. The decrease of $\tau'$was expected too, since it was demonstrated in Figure 12.b that for larger V_{loop} (which is proportional to t^*_{elu}) less tailing is observed.

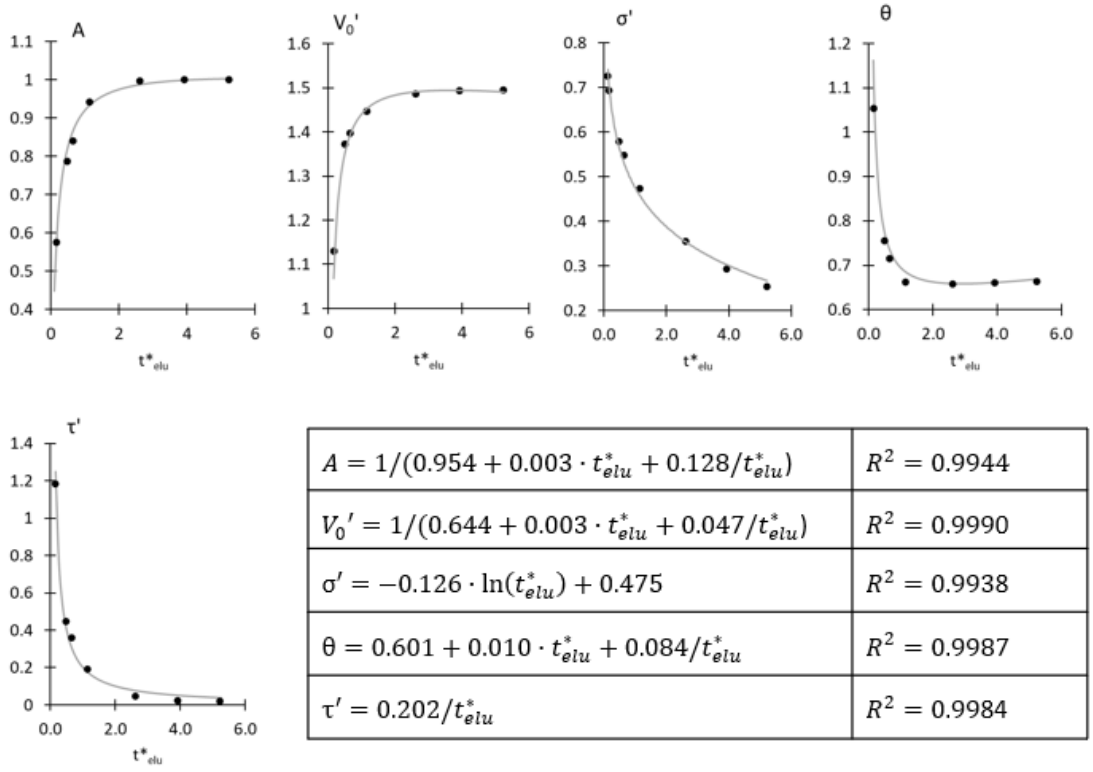

$A = 1/(0.954 + 0.003 \cdot t^*_{elu} + 0.128/t^*_{elu})$	$R^2 = 0.9944$
$V_0' = 1/(0.644 + 0.003 \cdot t^*_{elu} + 0.047/t^*_{elu})$	$R^2 = 0.9990$
$\sigma' = -0.126 \cdot \ln(t^*_{elu}) + 0.475$	$R^2 = 0.9938$
$\theta = 0.601 + 0.010 \cdot t^*_{elu} + 0.084/t^*_{elu}$	$R^2 = 0.9987$
$\tau' = 0.202/t^*_{elu}$	$R^2 = 0.9984$

Figure 41. Fit parameters from Eq. 29 for some t^*_{elu}. Black dots are from simulated peaks and gray solid lines are the empirical functions in the table.

Figure 42 shows a comparison between a peak, which was excluded from the fitting step to be used in the validation step, and the profile generated by Eq. 10 in combination with the empirical functions in Figure 33. The good agreement between both curves indicate that the modelling equations enables the generation of elution profiles in the studied t^*_{elu} range.

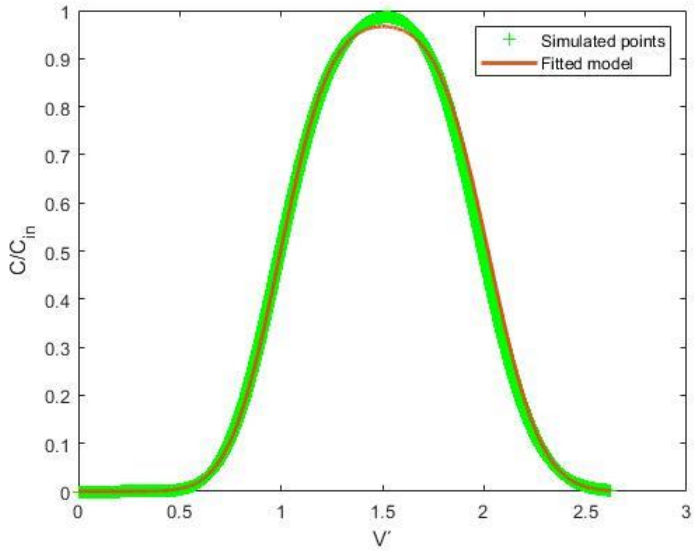

Figure 42. Elution profile for t^*_{elu}=1.95 and F_{elu}/F_{fill}=1 obtained from CFD simulations and the fitted model.

To sum up, in this section the mathematical model from [21] and [4] has been successfully applied in a limited t^*_{elu} domain for F_{elu}/F_{fill}=1, within a wide range of conditions, in a straight capillary operating in FIFO mode. It has also been verified that reproduces the elution profiles with an acceptable accuracy. Unfortunately, for lower t^*_{elu} the literature is not able to accurately describe the strongly tailing and sharp peak profiles making it not suitable to describe the FIFO elution profiles for the entire t^*_{elu}-range. However, this lower t^*_{elu} range is less relevant in practice as it corresponds to such very high elution flow rates, small loop volumes and D_{mol}-values which are seldom encountered in practice in 2D-LC.

5. Conclusions

In this project, a fitting function was obtained that enables the prediction of the peak variance in a F_{elu}/F_{fill} range between 1 and 80, and for any possible value of t^*_{elu} of peak eluting from a straight capillary operated in FIFO mode with a filling fraction of 0.5. In the case of large t^*_{elu}-values (i.e. low F_{elu}, large V_{fill} or D_{mol}, small loop radius), low peak variances are obtained, which may be explained by longer times for radial diffusion avoiding tail formation during elution. As t^*_{elu} decreases, peak variance increases due to tailing formation up to a point where it decreases again. Two hypotheses have been proposed and demonstrated to be feasible explaining this behavior: mass transfer entry length and the effect of the finite cut-off value.

Regarding the effect of increasing $F_{elu}/F_{fill,}$ it can be observed that for small t^*_{elu}-values σ_V^2/V_{fill}^2 grows because long tailings are formed, and slight differences in tailing affects peak variance significantly, whereas as t^*_{elu} increases the different curves converge at an intersection point (t^*_{elu}~0.025), from where σ_V^2/V_{fill}^2 decreases with higher F_{elu}/F_{fill} due to radial diffusion during filling step.

Loop filling fraction resulted to be an important parameter affecting peak variance in FIFO mode. A lower filling fraction means that sample needs to travel a longer distance in the loop at F_{elu}, hence more dispersion, whereas filling fraction over 0.5 results in breakthrough of the sample during filling step. Therefore, $V_{fill} = 0.5 \cdot V_{loop}$ seems to be the optimum filling fraction as it exhibits the minimal peak variance without sample loss.

The experimental results show a similar behavior as the numerical data when using a straight capillary setup for F_{elu}/F_{fill}=8 and 20. In F_{elu}/F_{fill}=1 a significant scatter in the experimental data was observed, which was found due to deviations of the intended filling fractions of 0.5 due to technical limitations. Unfortunately, it was not possible to investigate lower t^*_{elu}-values as these corresponded to impractical experimental conditions. Data from coiled capillary resulted in lower peak variances since secondary flow effects enhance radial dispersion.

Finally, the mathematical model developed by [21] and [4] has been successfully applied in a dimensionless form for F_{elu}/F_{fill}=1, for a wide range of conditions (t^*_{elu}= 0.012-5.22), in a straight capillary operating in FIFO mode. It has also been verified that reproduces the elution profiles with an acceptable accuracy.

6. Bibliography

[1] P. W. Carr and D. R. Stoll, “Two-dimensional liquid chromatography: Principles, practical implementation and applications,” *Agil. Tech. Note*, pp. 1–163, 2015.

[2] B. W. J. Pirok, D. R. Stoll, and P. J. Schoenmakers, “Recent Developments in Two-Dimensional Liquid Chromatography: Fundamental Improvements for Practical Applications,” *Anal. Chem.*, vol. 91, no. 1, pp. 240–263, 2019.

[3] A. Moussa, T. Lauer, D. Stoll, G. Desmet, and K. Broeckhoven, “Numerical and experimental investigation of analyte breakthrough from sampling loops used for multi-dimensional liquid chromatography,” *J. Chromatogr. A*, vol. 1626, p. 461283, 2020.

[4] S. L. Weatherbee, T. Brau, D. R. Stoll, S. C. Rutan, and M. M. Collinson, “Simulation of elution profiles in liquid chromatography – IV: Experimental characterization and modeling of solute injection profiles from a modulation valve used in two-dimensional liquid chromatography,” *J. Chromatogr. A*, vol. 1626, pp. 1–10, 2020.

[5] E. J. Hsieh, M. S. Bereman, S. Durand, G. A. Valaskovic, and M. J. MacCoss, “Effects of column and gradient lengths on peak capacity and peptide identification in nanoflow LC-MS/MS of complex proteomic samples,” *J. Am. Soc. Mass Spectrom.*, vol. 24, no. 1, pp. 148–153, 2013,.

[6] Dioumaeva, I., Choi, Seok-Bong, “Understanding Orthogonality in Reversed-Phase Liquid Chromatography for Easier Column Selection and Method Development,” *Appl. note, Agil. Technol. Inc.*, no. 1, 2010.

[7] I. François, K. Sandra, and P. Sandra, “Comprehensive liquid chromatography: Fundamental aspects and practical considerations-A review,” *Anal. Chim. Acta*, vol. 641, no. 1–2, pp. 14–31, 2009.

[8] D. R. Stoll, X. Li, X. Wang, P. W. Carr, S. E. G. Porter, and S. C. Rutan, “Fast, comprehensive two-dimensional liquid chromatography,” *J. Chromatogr. A*, vol. 1168, no. 1–2, pp. 3–43, 2007, doi: 10.1016/j.chroma.2007.08.054.

[9] D. R. Stoll, *Introduction to Two-Dimensional Liquid Chromatography—Theory and Practice*. Elsevier Inc., 2017.

[10] J. Pandohee, P. Stevenson, X.-R. Zhou, M. Spencer, and O. Jones, “Multi-Dimensional Liquid Chromatography and Metabolomics, Are Two Dimensions Better Than One?,” *Curr. Metabolomics*, vol. 3, no. 1, pp. 10–20, 2015.

[11] M. G. M. van de Schans, M. H. Blokland, P. W. Zoontjes, P. P. J. Mulder, and M. W. F. Nielen, “Multiple heart-cutting two dimensional liquid chromatography quadrupole time-of-flight mass spectrometry of pyrrolizidine alkaloids,” *J. Chromatogr. A*, vol. 1503, pp. 38–48, 2017.

[12] K. Sandra, M. Steenbeke, I. Vandenheede, G. Vanhoenacker, and P. Sandra, “The versatility of heart-cutting and comprehensive two-dimensional liquid chromatography in monoclonal antibody clone selection,” *J. Chromatogr. A*, vol. 1523, pp. 283–292, 2017.

[13] J. N. Fairchild, K. Horváth, and G. Guiochon, “Approaches to comprehensive multidimensional liquid chromatography systems,” vol. 1216, pp. 1363–1371, 2009.

[14] P. Jandera, *Comparison of various modes and phase systems for analytical HPLC*, vol. 8. 2020.

[15] D. R. Stoll, K. Shoykhet, P. Petersson, and S. Buckenmaier, “Active Solvent Modulation: A Valve-Based Approach To Improve Separation Compatibility in Two-Dimensional Liquid Chromatography,” 2017.

[16] J. F. Wendt *et al.*, *Computational fluid dynamics: An introduction*. 2009.

[17] B. R. Munson, T. H. Okiishi, W. W. Huebsch, Rothmayer, and A. P, *Fundamentals of Fluid Mechanics Seventh Edition*. 2013.

[18] S. a Socolofsky and G. H. Jirka, “Special topics in mixing and transport processes in the environment,” *Coast. Ocean Eng. Div.*, no. 5th Edition, p. 171, 2005.

[19] D. R. Stoll, E. S. Talus, D. C. Harmes, and K. Zhang, “Evaluation of detection sensitivity in comprehensive two-dimensional liquid chromatography separations of an active pharmaceutical ingredient and its degradants,” *Anal. Bioanal. Chem.*, vol. 407, no. 1, pp. 265–277, 2015.

[20] S. Deridder, G. Desmet, and K. Broeckhoven, “Numerical investigation of band spreading generated by flow-through needle and fixed loop sample injectors,” *J.*

Chromatogr. A, vol. 1552, pp. 29–42, 2018.

[21] P. Forssén, L. Edström, J. Samuelsson, and T. Fornstedt, "Injection profiles in liquid chromatography II: Predicting accurate injection-profiles for computer-assisted preparative optimizations," *J. Chromatogr. A*, vol. 1218, no. 34, pp. 5794–5800, 2011.

[22] Y. A. Çengel, *Heat and Mass Transfer: Fundamental & Applications*, 5th ed. Mc Graw-Hill, 2014.

[23] D. J. Auld, "Entrance length," 2005. http://www-mdp.eng.cam.ac.uk/web/library/enginfo/aerothermal_dvd_only/aero/fprops/pipeflow/node9.html (accessed Mar. 15, 2021).

[24] R. E. Hayes and J. P. Mmbaga, "Entry Length Effects for Momentum, Heat and Mass Transfer in Circular Ducts with Laminar Flow," vol. 93, no. March, pp. 863–869, 2015.

[25] A. Moussa, T. Lauer, D. Stoll, G. Desmet, K. Broeckhoven, "Modelling of analyte elution profiles and band broadening generated by interface loops used in multi-dimensional liquid chromatography," *J. Chromatogr. A*, in preparation.

[26] Y. Vanderheyden, K. Broeckhoven, and G. Desmet, "Comparison and optimization of different peak integration methods to determine the variance of unretained and extra-column peaks," *J. Chromatogr. A*, vol. 1364, pp. 140–150, 2014.